



RESEARCH REPOSITORY

*This is the author's final version of the work, as accepted for publication following peer review but without the publisher's layout or pagination.
The definitive version is available at:*

<https://doi.org/10.1016/j.oregeorev.2018.01.003>

Rojas, P.A., Barra, F., Deditius, A., Reich, M., Simon, A., Roberts, M. and Rojo, M. (2018)
New contributions to the understanding of Kiruna-type iron oxide-apatite deposits revealed by magnetite ore and gangue mineral geochemistry at the El Romeral deposit, Chile. *Ore Geology Reviews*

<http://researchrepository.murdoch.edu.au/id/eprint/40004/>

Copyright: © 2018 Elsevier B.V.
It is posted here for your personal use. No further distribution is permitted.

Accepted Manuscript

New contributions to the understanding of Kiruna-type iron oxide-apatite deposits revealed by magnetite ore and gangue mineral geochemistry at the El Romeral deposit, Chile

Paula A. Rojas, Fernando Barra, Artur Deditius, Martin Reich, Adam Simon, Malcolm Roberts, Mario Rojo

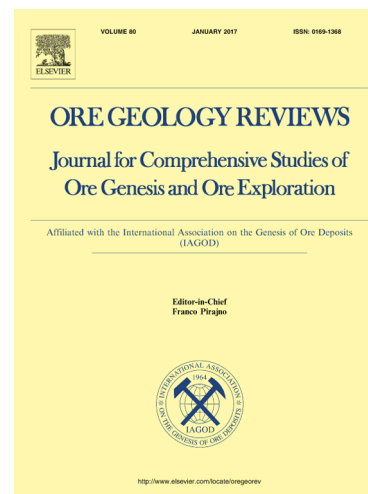
PII: S0169-1368(17)30698-4
DOI: <https://doi.org/10.1016/j.oregeorev.2018.01.003>
Reference: OREGEO 2448

To appear in: *Ore Geology Reviews*

Received Date: 13 September 2017
Revised Date: 2 January 2018
Accepted Date: 4 January 2018

Please cite this article as: P.A. Rojas, F. Barra, A. Deditius, M. Reich, A. Simon, M. Roberts, M. Rojo, New contributions to the understanding of Kiruna-type iron oxide-apatite deposits revealed by magnetite ore and gangue mineral geochemistry at the El Romeral deposit, Chile, *Ore Geology Reviews* (2018), doi: <https://doi.org/10.1016/j.oregeorev.2018.01.003>

This is a PDF file of an unedited manuscript that has been accepted for publication. As a service to our customers we are providing this early version of the manuscript. The manuscript will undergo copyediting, typesetting, and review of the resulting proof before it is published in its final form. Please note that during the production process errors may be discovered which could affect the content, and all legal disclaimers that apply to the journal pertain.



New contributions to the understanding of Kiruna-type iron oxide-apatite deposits revealed by magnetite ore and gangue mineral geochemistry at the El Romeral deposit, Chile

Paula A. Rojas¹, Fernando Barra¹, Artur Deditius², Martin Reich¹, Adam Simon³, Malcolm Roberts⁴, Mario Rojo⁵

¹ Department of Geology and Andean Geothermal Center of Excellence (CEGA), Universidad de Chile, Plaza Ercilla 803, Santiago, Chile.

² School of Engineering and Information Technology, Murdoch University, 90 South Street, Murdoch, Western Australia 6150, Australia.

³ Department of Earth and Environmental Sciences, University of Michigan, 1100 North University Ave, Ann Arbor, Michigan, USA.

⁴ Center for Microscopy, Characterisation and Analysis (CMCA), University of Western Australia, Crawley, Western Australia 6009, Australia

⁵ Compañía Minera del Pacífico (CAP), Pedro Pablo Muñoz 675, La Serena, Chile.

Revised version Dec, 2017

Ore Geology Reviews

Corresponding author:

Fernando Barra

Departamento de Geología, Universidad de Chile, Chile

fbarrapantoja@ing.uchile.cl

ABSTRACT

Iron oxide-apatite (IOA) or Kiruna-type deposits are an important source of iron and other elements including REE, U, Ag, and Co. The genesis of these deposits remains controversial, with models that range from a purely magmatic origin to others that involve variable degrees of hydrothermal fluid involvement. To elucidate the formation processes of this deposit type, we focused on the Chilean Iron Belt of Cretaceous age and performed geochemical analyses on samples from El Romeral, one of the largest IOA deposits in northern Chile. We present a comprehensive field emission electron microprobe analysis (FE-EMPA) dataset of magnetite, apatite, actinolite, pyroxene, biotite, pyrite, and chalcopyrite, obtained from representative drill core samples. Two different types of magnetite grains constitute the massive magnetite bodies: an early inclusion-rich magnetite (Type I); and a pristine, inclusion-poor magnetite (Type II) that usually appears as an overgrowth around Type I magnetite. High V (~2500-2800 ppm) and Ti concentrations (~80-3000 ppm), and the presence of high-temperature silicate mineral inclusions (e.g., pargasite, ~800-1020°C) determined by micro-Raman analysis indicate a magmatic origin for Type I magnetite. On the other hand, high V (2300-2700 ppm) and lower Ti (50-400 ppm) concentrations of pristine, inclusion-poor Type-II magnetite indicate a shift from magmatic to hydrothermal conditions for this mineralization event. Furthermore, the composition of primary actinolite (Ca- and Mg-rich cores) within Type-II magnetite, the presence of F-rich apatite and high Co:Ni ratios (>1-10) of late stage pyrite mineralization are consistent with a high temperature (up to 840°C) genesis for the deposit. At shallow depths of the deposit, the presence of pyrite with low Co:Ni ratios (<0.5) and OH-rich apatite which contains higher Cl concentrations relative to F record a dominance of lower temperature hydrothermal conditions (<600°C) and a lesser magmatic contribution. This vertical zonation, which correlates with the sub-vertical shape of the massive iron ore bodies, is concordant with a transition from magmatic to hydrothermal domains described in several IOA deposits along the Chilean Iron Belt, and supports a magmatic-hydrothermal model for the formation of the El Romeral. The close spatial and temporal association of the deposit with the Romeral Fault System suggests that a pressure drop related to changes in the tectonic stress had a significant impact on Fe solubility, triggering ore precipitation.

Keywords: Iron oxide-apatite; mineral chemistry; iron solubility model; El Romeral; northern Chile

ACCEPTED MANUSCRIPT

1. Introduction

Iron oxide-apatite (IOA) deposits, also known as Kiruna-type and magnetite-apatite deposits, are considered the Cu-deficient end-member of the iron oxide-copper-gold (IOCG) clan (Williams et al., 2005). Both of these deposit types are economically important as sources of commodities such as Fe, Cu, Au, U, and REE (Barton, 2014), making them a topic of scientific interest. These deposits are found in several metallogenic provinces around the world and formed throughout geologic time, from the Archean (e.g., Carajás Province, Brazil; de Melo et al., 2017) to early Proterozoic (e.g., Kiruna district, Sweden; Jonsson et al., 2013; Westhues et al., 2017), middle Proterozoic (e.g., Pea Ridge and Pilot Knob, USA; Day et al., 2016; Childress et al., 2016) to the Pliocene (e.g., El Laco, Chile; Makshev et al., 1988; Nyström and Henríquez, 1994; Naranjo et al., 2010). The genesis and potential genetic relationship between IOA and IOCG deposits has been subject of a long-standing controversy, where two main hypotheses have been proposed. The magmatic hypothesis invokes liquid immiscibility between a silicate melt and a conjugate Fe-rich melt with an important volatile component (Nyström and Henríquez, 1994; Naslund et al., 2002; Velasco et al., 2016; Tornos et al., 2016). The second hypothesis involves replacement of intermediate composition plutonic or volcanic units by hydrothermal fluids of non-magmatic (basinal brines, connate fluids) or magmatic origin exsolved from mafic intrusions (Menard, 1995; Rhodes and Oreskes, 1999; Rhodes et al., 1999; Sillitoe and Burrows, 2002; Dare et al., 2015). Recently, Knipping et al. (2015a, b) proposed a new model that reconciles the purely magmatic vs. hydrothermal viewpoints. This model states that the flotation and coalescence of primary magmatic magnetite-bubble pairs within a magma chamber is an efficient mechanism for magnetite ore concentration. The exsolved bubbles (i.e., magmatic-hydrothermal fluid) efficiently scavenge metals such as Fe, Cu and Au, as well as S, owing to the large positive fluid/melt partition coefficients for these elements (Chou and Eugster, 1977; Boctor et al., 1980; Simon et al., 2004; Williams-Jones and Heinrich, 2005; Simon and Ripley, 2011; Zajacz et al., 2012), as well as REE (Reed et al., 2000) and other metals (e.g., Ag; Simon et al., 2008) from the melt. Rapid ascent of the bubble-magnetite suspension through regional scale structures results in the formation of massive sub-vertical iron oxide ore bodies. The change from magmatic to hydrothermal conditions in magnetite is evidenced by characteristic trace element zoning

patterns and isotopic signatures that shift from heavy to lighter $\delta^{56}\text{Fe}$ and $\delta^{18}\text{O}$ values (Knipping et al., 2015a, b; Bilenker et al., 2016). Additionally, this model suggests a possible genetic link between IOCGs and IOA deposits, where an IOCG deposit could form at a shallower crustal level or at a distal lateral position from the IOA deposit (Reich et al., 2016; Barra et al., 2017).

In this contribution we present and discuss new mineral chemistry data for magnetite and associated sulfide and gangue minerals (i.e., pyrite, amphibole, pyroxene, biotite, and apatite) from El Romeral deposit in Chile that supports the model of Knipping et al. (2015a, b), pointing to a combination of efficient magmatic and hydrothermal processes of Fe concentration. The El Romeral is one of the largest IOA deposits in the Cretaceous Chilean Iron Belt, which extends ~1000 km along the Coastal Cordillera of northern Chile and contains >50 deposits with >40 Mt Fe (**Fig. 1**). Mineral phases including magnetite, apatite, actinolite, pyroxene, biotite, pyrite, and chalcopyrite were analyzed by using high-resolution, field emission electron microprobe analyzer (FE-EMPA) techniques. Additionally, micro-Raman spectroscopy was used to identify the nature of mineral inclusions within magnetite crystals in order to determine the crystallization history of the magnetite ore. Because the El Romeral and many other Chilean IOA deposits are intimately associated with transtensional structures within the Atacama Fault System, we further explore the effects of decompression on Fe solubility, and on magnetite ore precipitation.

2. Geologic background

The development of the mid-Cretaceous Chilean Iron Belt occurred under an extensional tectonic regime caused by renewed subduction on the western margin of Gondwana (Coira et al., 1982; Jaillard et al., 1990). These extensional conditions resulted in the formation of a subsiding trench-parallel magmatic arc and a back-arc basin (Brown et al., 1993; Scheuber et al., 1994; Charrier et al., 2007).

The El Romeral IOA deposit is located at the southern end of the Chilean Iron Belt, between latitudes 29°44'S and 29°42'S (**Fig. 1**). Resources have been estimated at about 450 Mt with a 28.3% iron grade (CAP Minería 2014 Annual Report) and up to 1.1%

vanadium (Dobbs, 1978). Mineralization is hosted by the late Jurassic to Neocomian La Liga Formation, which is an andesite lava flow from the Agua Salada Volcanic Complex (Emparán and Pineda, 2005). Emplacement of the magnetite ore bodies was controlled by the sinistral NNW strike-slip Romeral fault, which is an extension of the Atacama Fault System (AFS). The El Romeral deposit is limited to the west by the Romeral Diorite (129.0 ± 0.9 Ma U-Pb zircon age, Rojas, 2017) and to the east and north by the post-ore granitic to granodioritic Punta de Piedra intrusion (102.2 ± 2.0 Ma U-Pb zircon age, Rojas, 2017). The Cerro del Cobre monzogranite and sienogranite batholith (U-Pb zircon age of 126.5 ± 2 Ma; Emparán and Pineda, 2000) intrudes the volcanic sequences of La Liga Formation on the western side of the deposit (**Fig. 2**). Additionally, several NW to NNW post- and syn-ore diorite to granodiorite dikes have been described in the deposit (Bookstrom, 1977).

Three ore bodies have been identified in the El Romeral, from north to south: Cerro Norte, Cerro Principal, and Extensión Sur (**Fig. 2**; Espinoza, 2000). Cerro Norte comprises sub-vertical massive magnetite bodies with low phosphorous and sulfur, whereas Extensión Sur is composed of a massive and brecciated iron ore with higher contents of phosphorous and sulfur, possibly caused by the presence of abundant apatite and pyrite associated with the magnetite ore. Cerro Principal is the main ore body and comprises a massive, vertical magnetite body that contains minor actinolite. The massive magnetite ore body grades outward to disseminated magnetite, forming a transition zone with iron grades ranging between 22% to 45% Fe. Actinolite from the massive magnetite ore body yields radiometric $^{40}\text{Ar}/^{39}\text{Ar}$ ages of ca. 128 Ma (Rojas, 2017).

Brecciated rocks with magnetite clasts, which in some cases display plastic deformation, embedded in an actinolite matrix are observed near fault zones, particularly at the eastern and southern margins of the deposit (Espinoza, 2000). Late magnetite veinlets are also described cross-cutting the main ore bodies and the andesite host rocks.

3. Samples and Methods

Samples were collected from five drill cores along a NS transect in the Cerro Principal ore body (**Fig. 2**). Ten polished sections were inspected using a scanning electron

microscope (SEM), and nine of these samples were further analyzed by using a field emission electron microprobe analyzer (FE-EMPA). Two samples were further analyzed by using micro-Raman spectroscopy.

3.1 Scanning electron microscopy

Carbon coated polished sections were studied by using two different SEMs at the Centre for Microscopy, Characterisation and Analyses (CMCA), University of Western Australia, Perth, Australia: a TESCAN VEGA3 SEM with an acceleration voltage of 20 kV and a beam intensity of 10 nA equipped with an Oxford Instruments X-Max 50 silicon drift EDS system, and a FEI Verios XHR SEM with an acceleration voltage of 15 kV and a beam intensity of 1.6 nA. Backscattered-electron (BSE) images were obtained by using both instruments and qualitative energy dispersive X-ray (EDX) elemental maps of mineral inclusions in magnetite were obtained using the FEI instrument. For compositional maps, $\text{NaK}\alpha$, $\text{MgK}\alpha$, $\text{AlK}\alpha$, $\text{SiK}\alpha$, $\text{ClK}\alpha$, $\text{KK}\alpha$, $\text{CaK}\alpha$, $\text{TiK}\alpha$, $\text{MnL}\alpha$, and $\text{FeL}\alpha$ lines were monitored with an 80 mm² Oxford Instrument X-Max SDD EDX detector. AZtec and INCA software were used for measurements and data processing.

3.2 Electron microprobe analyses

Electron microprobe analyses were carried out at the CMCA, University of Western Australia by using a JEOL 8530F FE-EMPA equipped with five wavelength-dispersive crystal spectrometers and an optical microscope for focusing. Single-spot microanalyses were performed on carbon coated polished sections, with an accelerating voltage of 20 kV, a beam current of 50 nA and fully focused beam for magnetite; 25 kV, 40nA and focused beam for sulfides; 15kV, 15nA and focused beam for silicates; and 15kV, 15nA and beam size of 10 μm for apatite. The MAN correction method was used for the data acquisition and correction. Analytical conditions including counting time and standards are listed in the **Supplementary Materials (Table SM1)**. For magnetite and ilmenite Si, Al, Na, Mg, Ti, Ca, K, Fe, Cr, Ni, V, Mn, Zn, and Cu were analyzed, and interference corrections were performed for $\text{NaK}\alpha$, $\text{FeK}\alpha$, $\text{CrK}\alpha$, $\text{VK}\alpha$, and $\text{MnK}\alpha$. Sulfur, As, Sb, Fe, Se, Au, Te, Cu,

Pb, Ni, Co, Ag, Bi, Si, Pd, Hg, Re, Os, Pt, Cd, and Zn were measured in pyrite and line overlap corrections were carried out for $SK\alpha$, $AsL\alpha$, $FeK\alpha$, $SeL\alpha$, $TeL\alpha$, $PbM\alpha$, $BiM\alpha$, $HgL\alpha$, $ReL\alpha$, $OsL\alpha$, $PtL\alpha$, and $ZnK\alpha$. For silicate phases (actinolite, biotite, and pyroxene) F, Cl, Ca, Si, Mg, Al, Mn, Na, Ti, K, Cr, Fe, and V were analyzed and interference corrections were performed for $MnK\alpha$, $CrK\alpha$, $FeK\alpha$, and $VK\alpha$. Oxygen and H contents in hydrated silicates were calculated based on ideal formulas. Only total weight percent results between 97% and 103% were used, except for some silicates, where the stoichiometric method for O and H is not an accurate approximation; however, for these minerals only total concentrations between 90% and 103% are considered. Finally, F, Cl, Ca, P, Sr, La, Ce, Nd, Si, Mg, Al, S, Mn, Na, and As were measured in apatite grains and overlap corrections were made on $FK\alpha$, $ClK\alpha$, $PK\alpha$, $SrL\alpha$, $NdL\alpha$, $SiK\alpha$, $AlK\alpha$, $MnK\alpha$, and $AsK\alpha$. Quantitative wavelength dispersive X-ray (WDX) maps of Si, Al, Na, Mg, Ti, Ca, Fe, V, Mn, and S were obtained by using an acceleration voltage of 20 kV, a beam current of 50 nA and a counting time of 80 s/element for unknown samples. ZAF corrections were applied for all elements and interference corrections were performed for $FeK\alpha$ and $VK\alpha$ because of $MnK\beta$ and $TiK\beta$ overlap, respectively.

3.3 Micro-Raman Spectroscopy

Raman measurements were performed at the Department of Chemistry, Universidad de Chile, Santiago, by using a Renishaw micro-Raman (RM 1000) system, equipped with laser lines 514, 633, and 785 nm, a Leica microscope DMLM and an electrically cooled CCD camera. The Raman signal was calibrated to the 520 cm^{-1} line of Si wafer and a 50X objective. Laser power was less than 2 mW. The resolution was set to 4 cm^{-1} and 1-10 scans between 10 and 20s per accumulation. Spectral data were obtained using the 785 nm laser line and were recorded between 100 and 3500 cm^{-1} . Analytical data processing was performed with CrystalSleuth software (Laesch and Downs, 2006) and Origin software (OriginLab, Northampton, MA).

3.4 Magnetite precipitation modeling

Iron solubility modeling was performed by using the GEMS software (Kulik et al., 2013). A reported Fe concentration of 7.2 wt.%, along with a minimum bulk salinity of 35 wt.%, obtained in synthetic fluid inclusions from magnetite solubility experiments (Simon et al., 2004), were used as input data, considering speciation of Fe as FeCl_2 complexes. PSI/Nagra (Hummel et al., 2002) and SUPCRT92 (Johnson et al., 1992) thermodynamic data were used in the model. For FeCl_2 solubility and magnetite precipitation calculations, a temperature and pressure variation of 10°C and 20 MPa were used over a temperature and pressure range of 380°-620°C and 60-200 MPa, respectively.

4. Results

4.1 Magnetite textures, chemistry and mineral inclusions

The magnetite ore body at the El Romeral comprises an aggregate of massive magnetite (>95% modal) with actinolite found mainly at the margins of the ore body. Massive magnetite comprises four main types of magnetite (**Table 1 and Fig. 3**), which exhibit significant textural variations and inclusion types/arrangements with depth (**Fig. 4**). Inclusion-rich magnetite (Type I) surrounded by inclusion-poor magnetite (Type II) rims occur at the deeper parts of the system (**Fig. 4A**). At the margins and shallow portions of the massive ore bodies, the magnetite grains (Type III) have scarce inclusions and are chemically-zoned (**Fig. 4B**). This magnetite type can have fractures filled with pyrite and actinolite. Disseminated magnetite is also observed in the volcanic host rocks and in the Romeral Diorite. At depth, this disseminated magnetite is similar to Type I and II magnetite grains from the massive ore bodies, but at shallow depths, these crystals contain ilmenite exsolution lamellae or ilmenite-actinolite inclusions following magnetite crystallographic planes (**Figs. 4E, F**). A fourth magnetite textural type (Type IV) is represented by veinlets with inclusion-free magnetite that crosscut the massive magnetite ore body.

In Type I magnetite, inclusions are oriented (**Fig. 4C**) or randomly distributed. These are polycrystalline and one-phase inclusions, varying in size from 50 μm to a few nanometers (**Fig. 4D**). Some larger inclusions are composed by actinolite and Ti-bearing mineral phases (co-crystallizing phases)– mainly ilmenite and rutile– whereas smaller inclusions are

characterized by aggregates of rutile, ilmenite, titanite, chlorite, and/or phlogopite (**Figs. 5 and 6A**), as well as NaCl and pargasite with Ca, Al, Mg, and minor Ti, K, Cl, Na, and Mn. The latter phase is also associated with K-feldspar aggregates and titanite at lower depths (<150 m), or with ilmenite and rutile in deeper zones (>300 m). Euhedral Si-rich inclusions are observed in shallow samples (<100 m), which are aligned along magnetite crystallographic planes (**Fig. 6B**).

Several mineral inclusions were identified in Type I magnetite by using micro-Raman spectroscopy. These include ilmenite, titanite, rutile, clinocllore (**Fig. 7A**), calcite, phlogopite, tremolite, and pargasite (**Fig. 7B**). Euhedral prismatic Si-rich inclusions spectra coincide with the characteristic α -quartz peaks at 462, 355, and 206 cm^{-1} and do not agree with Si-rich glass or other polymorph quartz spectra (**Fig. 7C**).

Elemental WDS maps of Fe, V, Ti, Si, Al, and Mg for Type I and Type II magnetite are shown in **Figure 8**, and for Type III magnetite in **Figure 9**. Type I magnetite is slightly depleted in Fe and enriched in Si, Al, Mg, Ca, and slightly in Ti in comparison with Type II (**Fig. 8**). The Si, Al, Mg, and Ca enrichment is most likely caused by the abundant presence of silicate inclusions. Type III magnetite shows a distinct zoning with a Si-Al-Ca-Mg-Ti-Na-rich cores and Fe-rich rims (**Fig. 9**). A pronounced oscillatory zoning for Si is observed in rims on Type III magnetite grains. A less distinct oscillatory zoning is also observed for Al. On the other hand, vanadium is homogeneously distributed throughout all magnetite types.

Electron microprobe spot analyses were performed only on Type I and II magnetite because they are the more abundant types in the deposit (>95% modal) and form the massive iron ore (**Table 1**). Type I magnetite has between 100-1000 ppm Si, 80-3000 ppm Ti, 2500-2800 ppm V, 120-1000 ppm Ca, and 100-800 ppm Mn. For Type II magnetite trace element concentrations are between 100-5100 ppm Si, 50-400 ppm Ti, 2300-2700 ppm V, 130-600 ppm Ca, and 120-200 ppm Mn. Higher Cr (200 ppm) values are observed in inclusion-poor disseminated magnetite (Type II) associated with ilmenite and rutile aggregates at depth, along with high V (2800 to 3300 ppm) and Ti (200 ppm to 1.14 wt%) contents. Representative analyses for Type I and II magnetite are shown in **Table 2**, and all results are reported in **Table SM2**.

4.2 Sulfide elemental composition

In this study, we identified two main pyrite events: an Early Pyrite event, related to magnetite Type II, and a Late Pyrite event, associated with magnetite Type IV (**Fig. 3**). In the latter, chalcopyrite is in direct association with pyrite, and both can be found as disseminated crystals in host rocks, veinlets crosscutting the main iron ore bodies or surrounding Type I and Type II magnetite crystals in the main ore bodies.

Cobalt, Ni, and Cu concentrations in pyrite from the magnetite ore body and disseminated grains in the host rocks are shown in **Table 3**, and complete measurements for pyrite and chalcopyrite are reported in **Table SM3**. Analyzed pyrite grains are anhedral and correspond to a post-magnetite mineralization event (**Fig. 10A**), with the exception of one sample where the pyrite crystal is completely surrounded by inclusion-poor magnetite grains, suggesting a syn-formation with Type II magnetite (**Fig. 3 and 10B**). Pyrite is characterized by Co and Ni contents that range between 0.01-2.24 wt.%, and from 0.01-0.76 wt.% with a median of 0.07 wt.% and 0.17 wt.%, respectively. In some grains, high concentrations of Cu are detected reaching up to 1.56 wt.%. Arsenic, Ag, Au, and other elements were not detected by EMPA.

Chalcopyrite analyses indicate generally constant concentrations of S (34.8-37.5 wt.%) and Fe (29.3-36.6 wt.%), and slightly variable concentrations of Cu (28.3-34.7 wt.%). Zinc in chalcopyrite is relatively homogeneous with concentrations between 0.02 and 0.08 wt.%. Some spot analyses revealed minor concentrations of Se (500-700 ppm), Ag (400-500 ppm), Si (100-1200 ppm), Pd (300-600 ppm), Hg (500 ppm), and Cd (500 ppm).

4.3 Gangue mineral chemistry

4.3.1 Actinolite

The main gangue phases in the deposit are actinolite, pyroxene, quartz, apatite, biotite, chlorite, titanite, and calcite. Actinolite ($\text{Ca}_2\text{Mg}_{2.5-4.5}\text{Fe}^{2+}_{>0.5-2.5}\text{Si}_8\text{O}_{22}(\text{OH})$; Hawthorne et al. 2012) is the most abundant gangue mineral and is characterized by different textures and

mineral associations (**Fig. 3**). Actinolite I is paragenetically related to Type II magnetite with quartz and pyroxene within the inclusion-poor magnetite grains in the massive ore body (**Fig. 11A**). Large (up to cm-size) acicular crystals of actinolite (actinolite II) are intergrown with Type II magnetite (**Fig. 11B**), usually at the margins of the magnetite ore body. A third type of actinolite (actinolite III) is present in veinlets with chlorite and sulfides, mainly pyrite and minor chalcopyrite. Representative analyses of actinolite I, II, and III are reported in **Table 4** and **Table SM4**.

Actinolite I is Ca-rich (up to 9.30 wt.% Ca) with slightly more Fe (up to 11.44 wt.%) than Mg (up to 9.30 wt.%) and shows zoning with Ca and Mg-rich cores and Fe and Al-rich rims. Minor elements are Na (up to 0.19 wt.%), Mn, and V with a maximum concentration of 0.1 wt.% and 0.08 wt.%, respectively. Actinolite II is characterized by a high Mg content (up to 11.5 wt.%) in comparison with Ca (up to 9.83 wt.%) and Fe (up to 8.97 wt.%), along with a pronounced zoning with increasing Ca contents from core to rim. Detectable concentrations of F and Cl are observed in most samples, mainly in the grain cores. Sodium is also present and shows a sharp pattern with decreasing values from cores to rims. The calculated Fe numbers ($Fe\# = Fe/(Fe+Mg)$, molar) for all generations of actinolite vary from 0.18 to 0.36, with an average of 0.34 for actinolite I, 0.23 for actinolite II, and 0.23 for actinolite veinlets (actinolite III).

4.3.2 Pyroxene

Pyroxene is found in association with actinolite I within Type II magnetite grains, as previously mentioned (**Fig. 3**). Pyroxene corresponds specifically to Ca-clinopyroxene ($Ca(Mg,Fe)Si_2O_6$; Morimoto et al., 1988), which was also analyzed. Two compositionally different Ca-clinopyroxene are observed: (i) a V and K-rich augite with similar concentrations of Ca (~9.0 wt.%), Mg (~8.4 wt.%), and Fe (~11.6 wt.%), and (ii) a V and Ti-rich augite with similar concentrations of Ca (~22.9 wt.%) and Fe (~19.7 wt.%), and minor Mg (~0.02 wt.%). Both clinopyroxene are found in the same association with actinolite I and Type II magnetite. EMPA data for clinopyroxene are listed in **Table SM5**.

4.3.3 Biotite

Secondary biotite related to a final event of magnetite mineralization (Rojas, 2017) was also analyzed. Biotite ($\text{K}(\text{Mg,Fe})_2\text{AlAl}_2\text{Si}_2\text{O}_{10}(\text{OH})_2$) crystals have an eastonite composition ($\text{KMg}_2\text{AlAl}_2\text{Si}_2\text{O}_{10}(\text{OH})_2$; Rieder et al., 1998) with F and Cl replacing the hydroxyl site, and a considerable amount of Ti (up to 1.27 wt.%) and minor V contents (<0.07 wt.%). EMPA data for biotite are listed in **Table SM6**.

4.3.4 Apatite

Apatite is a minor mineral phase in this deposit compared to magnetite and actinolite. It is usually present as disseminated grains (**Fig. 12A**) or in sinuous veinlets that crosscut the main ore body at different depths (**Fig. 3**). In veinlets, apatite crystals are usually subhedral to anhedral and in contact with pyrite grains. These apatite grains can contain several sulfide and silicate inclusions (**Fig. 12B**). Its chemistry can be complex (general formula $\text{A}_5(\text{XO}_4)_3\text{Z}$, Sommerauer and Katz-Lehnert, 1985) with several substitutions. The A-site, occupied by Ca^{2+} , can host REE^{3+} , Eu^{+2} , and other trace elements such as Cd, U, Th, Sr, Ba, among others. The X site or P^{5+} allows the incorporation of S, Si, V, and As, while halogens (F and Cl), OH, and S can be hosted at the anionic Z site. Hydroxyl content was estimated by using stoichiometric approximation and assuming a fully occupied Z site. Two different apatite compositions are identified (**Tables 5** and **SM7**): (i) a subhedral to hexagonal, F-rich apatite found at depth (~300 m) (**Fig. 12A**), and (ii) an OH-rich apatite found at shallower levels (~50 m) (**Fig. 12B**). Fluorapatite has a F content of 1.72-2.01 wt.%, and Cl contents between 0.1 and 0.13 wt.%, whereas hydroxyapatite has a higher Cl (up to 0.24 wt.%) and lower F (200 and 140 ppm) concentration. Silica content in fluorapatite is <0.09 wt.%. In contrast, hydroxyapatite crystals have concentrations between 0.01 wt.% and 0.56 wt.%. Sulfur and Mn are also detected in both apatite types, but contents are higher in fluorapatite, i.e., 0.67 wt.% S and 0.11 wt.% Mn. In contrast, the maximum S content in hydroxyapatite is 0.02 wt.%, while Mn reaches 0.08 wt.%. Additionally, La, Ce, and Nd were detected in some spots analyses, mainly in fluorapatite, with La yielding between 570 and 270 ppm, Ce between 1300 and 270 ppm, and Nd from 230 to 500 ppm. No zoning was observed in apatite grains.

5. Discussion

5.1 A magmatic-hydrothermal origin of magnetite at the El Romeral

Several compositional diagrams that use minor and trace elements abundances in magnetite have recently been proposed to discriminate magnetite among different ore deposit types and help to elucidate the origin of iron oxides in a variety of ore systems (Dare et al., 2014; Dupuis and Beaudoin, 2011; Knipping et al., 2015b; Nadoll et al., 2012; Nadoll et al., 2014a). Regardless of the type of diagram used, the usefulness of these discriminant plots depends strongly on the accuracy of the analytical measurements, along with sample selection and on the rigorousness of the previous petrographic observations to distinguish textures, zonings, and the presence and nature of mineral inclusions that may affect magnetite chemical measurements by microbeam techniques. As described in the previous section, magnetite from El Romeral ore deposit contains abundant micron- to nano-scale mineral inclusions, particularly in the core of magnetite grains from the massive magnetite ore body (Type I magnetite). This textural type was also described by Nold et al. (2014) at Pilot Knob, a Proterozoic IOA deposit in Missouri, USA, and by Knipping et al. (2015a, b) for the Cretaceous Los Colorados IOA deposit, in the Chilean Iron Belt. The cited authors have interpreted the inclusion-rich magnetite cores as a common feature of primary (magmatic?) magnetite.

One of the most widely used discriminant diagrams was presented by Dupuis and Beaudoin (2011) and later modified by Nadoll et al. (2014a), who proposed the use of Al, Mn, Ti, and V abundances as a tool to distinguish magnetite from different mineral deposit types (**Fig. 13**). Most of the analyses for magnetite grain from El Romeral magnetite grains plot within and below the Kiruna field, which suggests that this field could be extended further to lower Al + Mn compositions (dashed line in **Fig. 13**).

Chemical data were divided into magnetite (disseminated and massive) with abundant inclusions (Type I), and inclusion-poor or pristine magnetite (Type II). Type II magnetite samples with high Cr contents and spatially related to ilmenite and rutile were excluded due to anomalous Ti concentrations, inferred as measurements affected by Ti-rich inclusions.

The data for Type II magnetite is confined to a restricted Ti+V range (0.24-0.7 wt.%) and to low Al+Mn (mostly <0.1 wt.%) concentrations, whereas Type I magnetite show a more widespread distribution (**Fig. 13**).

As mentioned previously, the V content is generally constant for all samples (~2500-3300 ppm), except for magnetite in veinlets where a single measurement yielded a lower V contents (1700 ppm). In contrast, the concentration of Ti in magnetite is more variable (~100-8000 ppm) possibly because of the presence of Ti-rich inclusions such as titanite, ilmenite and/or rutile. The widespread distribution of Type I magnetite analyses plausibly reflects that several probe measurements (spot size ~1 micron) are affected by the presence of nano- or micron-scale inclusions of different types (silicate-rich and Ti-rich inclusions). Type I magnetite measurements affected by the presence of inclusions correspond to spots where different “enrichments” are observed. Titanium enrichment coupled with high Ca values is related to titanite inclusions whereas Ti-Mn enrichment is related to ilmenite and rutile inclusions. The few samples that plot within the Porphyry field in **figure 13** are enriched in Al, which plausibly reflects a contribution from silicate inclusions, such as phlogopite, chlorite or amphibole.

Knipping et al. (2015a, b) reported geochemical data for several textural types of magnetite from the Los Colorados IOA deposit, Chile (**Fig. 1**). These authors recognized magnetite grains with high concentrations of [Ti+V] and [Al+Mn] that plotted at the boundary between the fields for Porphyry and Fe-Ti, V deposits. Knipping et al. (2015a, b) interpreted those compositions as magmatic magnetite. Texturally, the magmatic magnetite grains from Los Colorados contain abundant micron- to nano-scale inclusions, similar to those observed in Type I magnetite in the present study. In addition, Knipping et al. (2015a, b) recognized a decreasing trend in the concentrations of Ti and Al from magmatic magnetite cores to rims, which those authors interpreted to represent a post-magmatic hydrothermal event. When plotted on the magnetite [Ti+V] and [Al+Mn] discriminant diagram, the composition of these “transitional” magnetite grains define an almost linear trend from the border of the Porphyry/Fe-Ti, V fields, through the Porphyry field, and in to the Kiruna field. However, Knipping et al. (2015a, b) report that the compositions of magnetite from late stage hydrothermal veinlets plot in all six fields on the [Ti+V] vs.

[Al+Mn] diagram. A similar trend is observed for the different types of magnetite from the El Romeral, where high [Al+Mn] and [Ti+V] values are obtained for Type I massive magnetite that contains abundant silicate and Ti-rich inclusions, and “transitional” [Al+Mn] and [Ti+V] values are observed in Type I disseminated and Type II inclusion-poor magnetite grains.

Nadoll et al. (2014a, b) reported compositions for magnetite from different ore deposits of hydrothermal and igneous origin that revealed specific ranges for certain elements. These authors found that high Mg (>1 wt.%) and Mn (<100-50400 ppm) contents are distinctive of hydrothermal magnetite, whereas low Mg concentrations (<3940 ppm) and Mn contents between 102 and 12500 ppm are characteristic of igneous magnetite. At El Romeral, Type I magnetite grains have concentrations between ~100 and 3600 ppm Mg and between ~100 and 1500 ppm Mn, values that are consistent with an igneous magnetite composition. Additionally, V concentrations in the El Romeral magnetite (Types I and II) range between 2300 and 3300 ppm, which plot within the overlap of the igneous and high temperature hydrothermal range (**Fig. 14**). Similarly, Types I and II magnetite contain 100-1000 ppm Ti, with some samples reaching up to 8000 ppm, plausibly due to the presence of micron- and nano-Ti-bearing mineral inclusions. This range is consistent with a high temperature hydrothermal origin (<3500 ppm) and with the lowermost concentrations measured in igneous magnetite (50-97800 ppm). These ranges confirm a high temperature affinity for Type I and II magnetite at El Romeral.

Figure 14 shows the Ti vs. V diagram from Knipping et al. (2015b), where they show that magnetite compositions plot in the overlap area between the high temperature hydrothermal field and the igneous field. Inclusion-free zones in Type I magnetite from El Romeral, plot dominantly within this overlapping high-temperature hydrothermal – igneous area, with Ti and V values ranging between ~80-3000 ppm and ~2500-2800 ppm, respectively. The V concentrations (~2300-2700) of pristine, inclusion-poor, Type II magnetite grains from El Romeral are consistent with high-temperature hydrothermal magnetite and igneous magnetite; however, Type II magnetite grains have lower Ti concentrations (~50-400 ppm) that plot outside the hydrothermal field defined by Nadoll et al. (2014b) and Knipping et al. (2015b). These lower Ti concentrations for Type II magnetite from El Romeral suggest a

hydrothermal origin for the pristine, inclusion-poor magnetite, in contrast with a magmatic affinity for Type I magnetite.

Chromium was used by Knipping et al. (2015b) to discriminate magnetite from IOA, porphyry, IOCG, and Fe-Ti/V deposits. These authors showed that magnetite from IOA deposits has lower Cr concentration than porphyry and Fe-Ti/V deposits, and are enriched in V relative to IOCG deposits. The low Cr concentrations in magnetite from IOA deposits may reflect the high mobility of Cr^{6+} in high temperature hydrothermal fluids (James, 2003), or augite fractionation in the source magma for a magmatic-hydrothermal fluid, which depletes the melt in Cr. The elevated V contents (>500 ppm) of magnetite from IOA deposits are consistent with crystallization of magnetite at high temperatures and favorable $f\text{O}_2$. In **figure 15**, the Cr and V concentrations for magnetite from El Romeral are plotted along with fields based on the study of Knipping et al. (2015b). The data for Types I and II magnetite crystals from El Romeral plot in the IOA field except for a few analyses ($n = 4$, not plotted) from Type II magnetite grains that are affected by ilmenite inclusions, reaching a Cr concentration of ~240 ppm. Hence, our results for magnetite from El Romeral support the use of this plot as a discriminant diagram for magnetite deposit types.

5.2 Mineral inclusion phases in magnetite grains

Mineral inclusions are common features of igneous and hydrothermal minerals and their composition can provide important constraint on the genesis of the sample. Diverse types of mineral inclusions in magnetite from other IOA deposits have been reported including phosphates, silicates, and sulfides (e.g., Bau and Alexander, 2009; Knipping et al., 2015a, 2015b; Nadoll and Koeing, 2011; Nadoll, 2013; Nold et al., 2014). For the case of El Romeral, different mineral inclusions are described indicating formation conditions of the main ore event. In the deeper portions of the deposit, Type I magnetite from the massive dike contains several types of mineral inclusions such as titanite, rutile, ilmenite, and clinocllore in the outer zones of cores, and Ti-pargasite in the inner cores (**Fig. 7**). At 200 MPa, pargasite stability is estimated between ~800°C and ~1020°C (Jenkins, 1983), although stability can increase with the incorporation of Ti as it has been reported for kaersutite (Stewart, 1980). At similar pressure conditions, clinocllore breaks down at

~780°C (Staudigel and Schreyer, 1977). Thus, the presence of these mineral inclusions indicate a high temperature formation of Type I magnetite, specifically temperatures that fluctuate between 800 and 1020°C for magnetite cores, with decreasing temperatures towards outer areas of cores (below 780°C). At shallow parts of the deposit, Type I magnetite hosts rutile, phlogopite, K-feldspar, minor pargasite, and α -quartz inclusions, as determined by using micro-Raman (**Fig. 7**). The α -quartz inclusions are arranged as oriented prismatic euhedral crystals (**Fig. 6B**), following magnetite crystallographic planes. The presence of α -quartz may be relevant since most Si-rich domains in magnetite have been attributed to the presence of Si in solid solution and/or small silicate inclusions (Newberry et al., 1982; Huberty et al., 2012). It is likely that crystal habit and orientation of α -quartz inclusions may indicate exsolution processes related to slow cooling rates, although hydrothermal crystallization of quartz along microfractures and/or inclusion phase changes during cooling or alteration cannot be ruled out.

5.3 Formation conditions for silicate phases

Three different generations of actinolite were analyzed: (i) actinolite (I) grains included in Type II magnetite and in contact with clinopyroxene and quartz (**Fig. 11A**), (ii) late pegmatitic actinolite (II) intergrown with Type II magnetite and located at the margins of the magnetite ore bodies (**Fig. 11B**), and (iii) secondary actinolite from veinlets and in disseminated aggregates, linked to the final hydrothermal sulfide event (**Fig. 3**). The first two types of actinolite associated with Type II magnetite show two distinct patterns in a Ca-Mg-Fe diagram (**Fig. 16**). Primary or early actinolite (I) shows a trend from slightly Ca- and Mg-rich cores to lower Ca concentration and higher Fe contents towards the rims. In contrast, late pegmatitic actinolite crystals display a more disperse pattern with increasing Ca concentrations from core to rims. The strong difference between these two patterns is consistent with the presence of two distinct actinolite generations. Further, the early actinolite I trend at the El Romeral is consistent with experiments that indicate a compositional, lower temperature re-equilibration with Fe-rich and Ca-poor cummingtonite overgrowths on the original high-temperature tremolite (Lledo and Jenkins, 2008). However, the more pronounced Ca depletion reported by Lledo and Jenkins (2008),

compared to El Romeral actinolite crystals, may be associated with the miscibility gap between actinolite and cummingtonite. The latter has an upper stability temperature of 840°C at 5 kbar, temperature that was reached during the first steps of the experimental re-equilibration of tremolite, generating early and strong cummingtonite nucleation (Lledo and Jenkins, 2008).

Published experimental data and thermodynamic modeling indicate that actinolite with Fe-numbers in the range of 0 to 0.4 are stable at 750°-900°C (Lledo and Jenkins, 2008). These authors determined experimentally that actinolite (Fe#=0.22) breaks down to clinopyroxene, orthopyroxene, quartz, and water at 780°-850°C and 1-4 kbar. This mineral assemblage (i.e., actinolite, clinopyroxene, orthopyroxene, quartz) is similar to that observed for the early actinolite (I) event in samples from El Romeral, and the compositional variations in high-temperature amphibole are concordant with the pattern obtained for actinolite (I) samples from El Romeral. These observations are consistent with a magmatic origin for this mineralization. Furthermore, the low Fe-numbers for the three types of actinolite (Type I=0.34; Type II=0.23; Type 3=0.23) in samples from El Romeral are consistent with actinolite crystallization at high-temperatures (i.e., circa magmatic temperatures). The relationship between temperature and actinolite Fe-number, which was experimentally determined by Lledo and Jenkins (2008) for amphibole with 1.7-2.0 a.p.f.u Ca, yield temperatures ranging from 735-805°C and 770-840°C at 1 and 2 kbar respectively, for the actinolite I and II events associated with Type II magnetite, as well as for actinolite III associated to a later veinlet event. We note that a magmatic origin for actinolite associated with magnetite in the Los Colorados IOA deposit established based on the O and H isotope composition of actinolite (Bilenker et al., 2016), and together with the data from El Romeral supports a magmatic-hydrothermal origin (i.e. crystallized from the exsolution of a magmatic fluid, along with a possible contribution of magmatic microlite) for IOA deposits.

Actinolite (I) is observed between magnetite crystals along with quartz and augite (**Fig. 11A and 3**). Microprobe data indicate that this augite has a considerable amount of V (up to ~0.4 wt.%, **Table SM5**), and some augite grains are enriched in Ti (0.01-0.4 wt.%). Vanadium and Ti contents are, in some cases, higher than those reported for magnetite,

consistent with crystallization from a V-Ti-rich fluid. Augite grains show a dominant Mg-rich composition with Fe-rich patches, indicating changes in composition and/or external conditions during crystallization, variations that are also observed in actinolite and that are attributed to temperature fluctuations.

5.4 Late magmatic stage of apatite formation

Apatite is a common accessory mineral in many rock types and is a ubiquitous phase in IOA deposits. Elemental accommodation is strongly dependent on external conditions, allowing the use of apatite as a powerful petrogenetic indicator and as a fluid tracer (Webster and Piccoli, 2015). Particularly, halogen concentrations in apatite are considered a good monitor of volatile fugacity during magmatic-hydrothermal crystallization (Nash, 1984). Based on halogen content, two types of apatite are recognized: a F-rich (1.72-2.01 wt.%) apatite confined to deeper samples in the deposit, and a OH-rich apatite with a high Cl content (up to 0.24 wt.%), associated with apatite veinlets at shallower depths in the deposit. Petrographic descriptions and BSE images (**Fig. 12**) of these apatite crystals show that these crystals are pristine with no signs of alteration or disequilibrium/replacement textures, hence, we interpret these chemical variations as primary features. **Figure 17** shows the compositional fields for apatite from different sources (igneous, hydrothermal, and sedimentary), and the results for apatite grains from El Romeral, with F-apatite grains plotting in the ore-forming intrusive field. Igneous apatite usually contains higher F concentrations over Cl (Webster and Piccoli, 2015); apatite containing more than 3.5 wt.% Cl is very rare in igneous rocks (Webster and Piccoli, 2015) due to the smaller radius (1.33\AA) and higher compatibility of F^- in apatite. In contrast, the larger Cl anion (1.81\AA) preferentially partitions into the fluid phase, resulting in a trend where igneous apatite progressively becomes depleted in F and enriched in Cl as hydrothermal conditions become more predominant (**Fig. 17**). This trend is observed at the El Romeral, with F-rich apatite found at depth and hence formed at higher temperature than OH-rich Cl-apatite, which is found at shallow depths. It follows then, that F-apatite formed at a late magmatic stage (Piccoli and Candela, 1994), whereas OH-apatite found in veinlets associated with the late sulfide event are of hydrothermal origin. Incorporation of OH over Cl in apatite at the El

Romeral may have been controlled by the pH of a deep and high temperature acidic hydrothermal fluid (Zhu and Sverjensky, 1991; Kusebauch et al., 2015).

Apatite composition was used to estimate halogen contents in a silicate melt and exsolved volatile phase. Thus, considering an igneous origin for F-apatite at the El Romeral, some compositional calculations can be performed. Assuming a temperature of 800°C for the actinolite event associated with F-apatite crystallization (Lledo and Jenkins, 2008), and a corresponding pressure of 200 MPa, the molality of HCl can be obtained using the following equation from Piccoli and Candela (1994):

$$m_{\text{HCl}}^{\text{aq}} \sim \frac{X_{\text{ClAp}}^{\text{Ap}}}{X_{\text{HAp}}^{\text{Ap}}} \cdot \frac{1000}{8} \cdot \frac{1}{10^{[0.04661 + \frac{2535.8}{T} + \frac{0.0303 \cdot (P-1)}{T}]}}$$

where $X_{\text{ClAp}}^{\text{Ap}}$ and $X_{\text{HAp}}^{\text{Ap}}$ are the mole fractions of Cl and OH in apatite, respectively, T is the apatite crystallization temperature in Kelvin and P is pressure in bars. A hydrochloric acid molality ranging between 0.0609 and 0.1622 was obtained for the magmatic volatile phase when F-apatite crystallized. If we assume that the melt has a metaluminous composition, the approximation of HCl:Cl ratio after Shinohara (1987) can be employed ($\log(\text{HCl}/\Sigma \text{Cl})^{\text{aq}} = -0.63 - 0.00035 \cdot P(\text{bars})$) to determine the concentration of Cl in the volatile phase. Following this approach, the volatile phase contained a maximum of 6.2 wt.% Cl. By using an aqueous phase/melt partition coefficient of 43.35 for Cl (Shinohara, 1987) at 1.2 kbar and 810°C, a Cl content of about 1000-1400 ppm was obtained for a melt in equilibrium with F-apatite. Following Piccoli and Candela (1994), and considering a volatile/melt partition coefficient of 0.184 for F (Webster, 1990), concentrations of F in the volatile phase and in the melt were calculated, obtaining values of 8.1-11.0 ppm and ~44-60 ppm, respectively. The low F/Cl ratio in melt may indicate that F-apatite scavenged F from the melt resulting in higher residual Cl content. Moreover, low Cl content in volatile phase (6.2 wt.%) in contrast with high salinity generally associated with these systems (35 wt.% NaCl_{eq}) may also suggest that F-apatite crystallized at a different magmatic stage. This event may be related to a late-stage exsolution of a low salinity (~6 wt.% NaCl_{eq}) fluid, unlike a prior event of single-phase fluid exsolution that at the solvus intersection will form an hypersaline (35 wt.% NaCl_{eq}) Fe-rich fluid and a low-density aqueous vapor.

Chlorine concentrations in melt and volatile phase are concordant with the incompatible behavior that characterizes this element.

5.5 Hydrothermal sulfide stage

Pyrite is an ubiquitous phase in mineral deposits, and in IOA deposits pyrite is the most common sulfide mineral, frequently with subordinate amounts of chalcopyrite. Pyrite has the capacity to incorporate important and variable concentrations of metals and metalloids of economic relevance such as Au, Ag, Cu, Pb, Co, Ni, Zn, As, Sb, Te, Tl, Bi, among others (e.g., Cook and Chryssoulis, 1990; Huston et al., 1995; Reich et al., 2005; Large et al., 2009; Deditius et al., 2014; Reich et al., 2016), in both solid solution and/or nanoparticulate phases. The El Romeral pyrite contains <1.0 wt.% of Co and Ni (**Table 3**). Cobalt shows a negative correspondence with Fe (**Fig. 18A**), which suggests substitution of Co by Fe in octahedral sites, as well as for Zn where a substitution of Fe²⁺ for Zn²⁺ may be suggested. In contrast, Ni does not follow a correlation with Fe or Co (**Fig. 18B**), a pattern previously reported by Reich et al. (2016) for Los Colorados pyrite, and that is suggestive of a complex and heterogeneous incorporation of Ni. Copper content in pyrite is scarce, and its presence could be related to chalcopyrite nanoparticles (Reich et al., 2016), or solid solution incorporation by replacement of Fe through a coupled substitution with As (Radcliffe and McSween, 1969; Pacevsky et al., 2008). However, no significant As was detected by microprobe analyses. Selenium, Pd, and Hg contents are associated with the presence of nanoparticles or with solid solution incorporation where Se replaces S isovalently, an incorporation enhanced at low temperature conditions (Huston et al., 1995), and Pd or Hg substitutes for Fe.

The Co:Ni ratio is a useful tool employed as a petrogenetic indicator in different deposit types (Loftus-Hills and Solomon, 1967; Bajwah et al., 1987; Bralia et al., 1979; Mookherjee and Philip, 1979). A high Co:Ni ratio (>1) in pyrite indicates a magmatic-hydrothermal affinity, associated with high-temperature mafic sources (Bajwah et al., 1987). A low Co:Ni ratio (i.e., <1.0) indicates a sedimentary or diagenetic origin for pyrite (Loftus-Hills and Solomon, 1967; Campbell and Ethier, 1984; Koglin et al., 2010).

Additionally, several authors have defined compositional fields for pyrite from different deposit, based on its Co and Ni content (**Fig. 19**).

Pyrite from El Romeral yielded a wide range of Co and Ni concentrations within different grains, possibly due to the existence of different events of sulfide mineralization. Previous petrographic studies on El Romeral samples defined three main sulfide events, a syn-ore event associated with Type I magnetite, a later event related to Type II magnetite, and a post-magnetite mineralization event related to hydrothermal veinlets (Rojas, 2017). Concordant to these observations, most of the samples plot above a Co:Ni ratio of 0.5, reflecting a hydrothermal origin for low Co:Ni values (~ 0.5) and magmatic-hydrothermal sources for high Co:Ni ratios (> 1.0), particularly for one sample with a high Co content (2.24 wt.%), corresponding to a pyrite related to Type II magnetite (Early Pyrite event; **Fig. 3, 10B and 18**). Lower Co:Ni ratios (< 0.5) are measured for pyrite disseminated in host rocks and for a late event of pyrite veinlet mineralization (Late Pyrite event; **Figs. 3 and 18**), which crosscut the magnetite dike at shallow levels, suggesting a greater contribution of meteoric or diagenetic fluids at upper levels.

Furthermore, there is a partial overlap for pyrite from El Romeral and pyrite from the Los Colorados deposit (Reich et al., 2016); however, most analyses of pyrite from El Romeral plot in the IOCG field, which is consistent with a hydrothermal origin for the main sulfide event and a probable magmatic-hydrothermal source for pyrite associated with Type II magnetite mineralization (**Fig. 10B**). The sulfur isotope composition of pyrite from El Romeral fingerprints a magmatic-hydrothermal source for sulfur in the El Romeral deposit ($\delta^{34}\text{S}$ for pyrite ranges from -0.8 to 2.9 ‰; Rojas, 2017).

5.6 Late magnetite mineralization event at El Romeral

A late magnetite mineralization event is associated with post-ore dikes at the El Romeral. This event has been dated at ~ 118 Ma ($^{40}\text{Ar}/^{39}\text{Ar}$ in hydrothermal biotite, Rojas et al., 2017), which is 10 Ma younger than the main magnetite event (~ 127 Ma, $^{40}\text{Ar}/^{39}\text{Ar}$ in actinolite II, Rojas, 2017). Biotite grains associated with this younger mineralization event have an eastonite composition, with predominant Fe content over Mg, and high Al

concentrations. By using the Ti-in biotite geothermometer proposed by Henry et al. (2005) in biotite:

$$T = ([\ln(\text{Ti}) - a - c(X_{\text{Mg}})^3]/b)^{0.333}$$

where T is temperature in °C, Ti (apfu) is calculated by a normalization to 22 O, and a, b and c are -2.3594, 4.6482e-9 and -1.7283, respectively, a temperature range between 560°C and 637°C was obtained for late-stage biotite from El Romeral.

The halogen content in biotite can be used to estimate the fugacity ratio ($f_{\text{H}_2\text{O}}/f_{\text{HCl}}$)^{fluid} following Munoz (1992):

$$\log(f_{\text{HF}}/f_{\text{HCl}})^{\text{fluid}} = \log\left(\frac{X_{\text{F}}}{X_{\text{Cl}}}\right) - \frac{1000}{T}(1.22 + 1.65X_{\text{Mg}}) + 0.25$$

$$\log(f_{\text{H}_2\text{O}}/f_{\text{HCl}})^{\text{fluid}} = \log\left(\frac{X_{\text{OH}}}{X_{\text{Cl}}}\right) + \frac{1000}{T}(1.15 + 0.55X_{\text{Mg}}) + 0.68$$

$$\log(f_{\text{H}_2\text{O}}/f_{\text{HF}})^{\text{fluid}} = \log\left(\frac{X_{\text{OH}}}{X_{\text{F}}}\right) + \frac{1000}{T}(2.37 + 1.1X_{\text{Mg}}) + 0.43$$

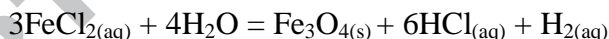
where X_{OH} , X_{Cl} , X_{F} stand for mole fractions of OH, Cl and F in biotite, respectively, X_{Mg} is calculated as (sum of Mg)/(sum of octahedral cations number) and T is the equilibration temperature in Kelvin between hydrothermal fluid and biotite. A temperature range between 550°C and 650°C was used for the fugacity ratio estimation based on the Ti-in biotite geothermometry results. Calculated fugacity ratios (**Fig. 20**) indicate two distinct trends: an increasing $\log(f_{\text{HF}}/f_{\text{HCl}})^{\text{fluid}}$ from -2.6 to -1.6 with increasing temperature (**Fig. 20A**); and a decreasing fugacity ratio with increasing temperature, including $\log(f_{\text{H}_2\text{O}}/f_{\text{HCl}})^{\text{fluid}}$ between 4.5 and 5.0 (**Fig. 20B**) and a $\log(f_{\text{H}_2\text{O}}/f_{\text{HF}})^{\text{fluid}}$ that ranges from 5.6 to 6.6 (**Fig. 20C**). These trends reflect the behavior of halogens with changing temperature, suggesting that f_{HF} increases with increasing temperature, yielding higher $\log(f_{\text{HF}}/f_{\text{HCl}})^{\text{fluid}}$.

These model results based on mineral compositions in samples from El Romeral indicate that: (i) the hydrothermal fluid at this late magnetite stage was relatively Cl-rich, and (ii) the late-stage biotite and associated secondary magnetite crystallized in the presence of a hydrothermal fluid characterized by high $f_{\text{H}_2\text{O}}/f_{\text{HCl}}$ and $f_{\text{H}_2\text{O}}/f_{\text{HF}}$ ratios. The model

fugacity ratios obtained for biotite crystals from El Romeral are similar to fugacity ratios reported for porphyry Cu systems (Bao et al., 2016), and are consistent with the notion that the final magnetite event at the El Romeral formed from a hydrothermal fluid exsolved from a magmatic source, i.e., the post-mineralization dikes.

5.7 Hydrothermal transport of Fe as a function of pressure

The sum of the data for samples from El Romeral indicate that the iron was probably derived from the Romeral Diorite and was transported by hydrothermal fluids of magmatic origin. Data from natural systems and experimental studies demonstrate that hydrothermal fluids are enriched in Fe over a wide range of temperature and pressure, and that the concentration of Fe is positively correlated with the Cl content of the fluid (Chou and Eugster, 1977; Heinrich et al., 1992; Audétat et al., 2000; Simon et al., 2004; Williams-Jones and Heinrich, 2005). Considering that El Romeral and all IOA deposits are fundamentally magnetite ore bodies, it is important to assess the ability for a hydrothermal fluid to transport a sufficient quantity of Fe to form an IOA deposit. Published studies indicate that FeCl_2 is the main dissolved complex of Fe in supercritical chloride bearing aqueous solutions (Chou and Eugster, 1977; Boctor et al., 1980), and that the precipitation of magnetite from an Fe-bearing hydrothermal fluid occurs by the following reaction:



We do not have an independent constraint on the total salinity of the hydrothermal fluid responsible for mineralization at the El Romeral. Knipping et al. (2015a) report the presence of halite-bearing fluid inclusions in magnetite rims for samples from the Los Colorados IOA deposit that are identical to Type II magnetite described in the present study. These authors report that the presence of halite indicates a minimum salinity of 35 wt.% NaCl_{eq} based on experimental data summarized in Bodnar and Vityk (1994). Thus, we used a fluid salinity of 35 wt.% NaCl_{eq} to model the solubility of magnetite as a function of pressure and temperature (**Fig. 21**). Experimental data at 800°C demonstrate that pressure plays an important role controlling magnetite solubility (Simon et al., 2004). Considering that the El Romeral and most magnetite-apatite deposits in the Chilean Iron

Belt are genetically related to major transtensional fault systems, particularly to sinistral driven Riedel shear zones, the effect of pressure on magnetite solubility is likely a crucial control on mineralization. In **figure 21**, the model results for magnetite solubility shows a strong dependence on pressure, especially at temperatures between $\sim 450^\circ$ and 620°C . The model results show that the solubility of FeCl_2 in aqueous fluid decreases significantly with decreasing pressure (**Fig. 21A**), which results in the precipitation of magnetite (**Fig. 21B**). The results also indicate that the rate of decompression affects the efficiency of magnetite precipitation. For example, a FeCl_2 -bearing hydrothermal fluid at 600°C will precipitate $\sim 50\%$ more magnetite at 100 MPa compare with the volume of magnetite precipitated at 120 MPa. Thus, for hydrothermal fluid with a given quantity of Fe dissolved as FeCl_2 , rapid decompression favors formations of a larger magnetite ore body.

5.8 A magmatic-hydrothermal model for the El Romeral

The data presented in this study show that the evolution of the El Romeral Fe deposit was characterized by different conditions and formation processes, leading to significant textural and chemical variations at both macro- and micro-scale.

The presence of a distinct textural and chemical variation between core and rims may be explained by a transition from magmatic to magmatic-hydrothermal conditions. Similar observations were reported by Knipping et al. (2015a, b), who proposed a magmatic-hydrothermal flotation model for the formation of IOA deposits (**Fig. 22**). Type I magnetite cores identified in the present study are consistent with crystallization of magnetite microlites from a silicate melt. Crystal surfaces of magnetite serve as nucleation sites to promote the exsolution of a magmatic-hydrothermal fluid from the silicate melt (**Fig. 22A**) (Hurwits and Navon, 1994; Gualda and Ghiorso, 2007). The exsolved fluid phase efficiently scavenges Cl, Fe and other metals from the silicate melt owing to the large fluid/melt partition coefficients for these elements (Zajacz et al., 2008). The small diameter of the magnetite microlites allows them to be entrained by the exsolved fluid phase, and a positive buoyancy force promotes ascent of the magnetite-bubble pairs through the magma body (**Fig. 22B**). Ascent of the magnetite-bearing magmatic-hydrothermal phase is focused along the pre-existing transtensional fault system. A sharp decrease in pressure triggers

precipitation of hydrothermal magnetite, evidenced by the presence of Type II inclusion-poor magnetite rim (**Fig. 22C**). The pronounced compositional zoning observed in pristine Type III magnetite crystals (**Figs. 4B and 9**), including increasing Si, Al, and Mg contents from rims to cores reflects fluctuating conditions affecting hydrothermal fluid composition.

Inclusion-poor hydrothermal Type II magnetite precipitates with minor pyrite and pyroxene, actinolite and quartz. Some of these mineral phases may have been transported as microlites or as mineral phases crystallized from the magmatic-hydrothermal fluid during ascent (**Fig. 22C**). At the margins of the dike-shaped ore body, pegmatitic actinolite (II) crystals formed, texturally related to this secondary hydrothermal event. Actinolite data reflect two different compositional trends: (i) early actinolite (I), related to pyroxene and quartz, with decreasing Ca and Mg contents and increasing Fe detected values from core to rims, and (ii) secondary pegmatitic actinolite (II) with increasing Ca contents from core to rim. These different trends are concordant with actinolite crystallization from two different events. Furthermore, the first trend is very similar to the compositional variation reported by Lledo and Jenkins (2008) for magmatic tremolite with decreasing temperature, supporting a high temperature origin (735°-805°C and 770°-840°C at 1 and 2 kbar, respectively) for the two actinolite events. Based on this mineralogy and its association with inclusion-poor magnetite, a temperature <840°C is defined for Type II magnetite mineralization.

Late pulses of hydrothermal fluid possibly related to late dikes are evidenced by the presence of magnetite and sulfides+chlorite veinlets that crosscut the main magnetite ore bodies. Lower V contents (1700 ppm) in the late-stage magnetite (Type IV magnetite) support the notion of a minor magmatic contribution for this stage compared to primary magnetite from the massive ore body (V content ranging between 2300-2800 ppm). The concentrations of Co and Ni in pyrite from the main mineralization event, where the Co/Ni ratio in pyrite is >0.5 and, as high as >10, are consistent with a mafic magmatic source for the magmatic-hydrothermal ore fluids. On the other hand, Co/Ni ratio <0.5 indicate a contribution of non-magmatic fluid(s) for late stage mineralization at shallow level of the deposit. A final stage of magnetite mineralization spatially related to hydrothermal biotite crystals is also reported, possibly associated with post-mineralization dikes (Rojas, 2017).

Conclusions

This study presents and interprets new geochemical data from the El Romeral IOA deposit, located in the Cretaceous Chilean Iron Belt (CIB), in order to better understand the genesis of one of the largest magnetite-apatite ore bodies in the CIB. Microprobe analyses, in combination with petrological studies, SEM and micro-Raman data, reveal two main mineralization events: (i) a first magnetite mineralization (Type I) represented by high-temperature, inclusion-rich magnetite cores at deep levels of the deposit and, at shallow levels of the deposit, by magnetite cores or disseminated crystals with α -quartz inclusions oriented along crystallographic planes evidencing a slow cooling system; and (ii) a second magnetite event recognized as inclusion-poor pristine magnetite (Type II), usually surrounding primary magnetite cores. Both events are characterized by magnetite that is enriched in V (~2300-2800 ppm), and has variable Ti concentrations (~50-3000 ppm). High Ti contents (~80-3000 ppm) in primary magnetite cores, coupled with an assemblage of micron- to nano-scale high-temperature (800°-1020°C) mineral inclusion assemblage identified in magnetite cores, are consistent with a magmatic origin for the first magnetite mineralization event. On the other hand, high V (~2300-2700 ppm) and lower Ti (~50-400 ppm) contents, along with marked zonations in magnetite crystals found at shallow depths of the deposit, are consistent with hydrothermal precipitation of magnetite from a magmatic-hydrothermal fluid with strongly fluctuating composition as a result of decompression and decreasing temperature.

Actinolite crystals at deeper levels of the deposit yield low Fe-numbers, reflecting temperatures of crystallization between 735° and 840°C, which is consistent with crystallization from a high-temperature hydrothermal fluid. The compositions of pyrite and apatite also record a distinct change from magmatic-hydrothermal fluid to lower-temperature hydrothermal fluids. This trend is reflected in Co:Ni ratios in pyrite, where deeper early pyrite mineralization yields ratios mostly ≥ 0.5 , and shallow, late stage pyrite yields lower ratios. Additionally, the abundances of F, Cl and OH in apatite vary strongly with depth, where F-apatite occurs in deeper zones of the deposit and OH-apatite with higher Cl contents occurs in veinlets at shallow levels.

The Fe solubility model presented here shows that magnetite precipitation occurs by decompression at temperatures $\geq 380^{\circ}\text{C}$. Iron oxide-apatite deposits in the Chilean Iron Belt are spatially associated with major transtensional fault zones (i.e., the Atacama Fault Zone), and the model results are consistent with a strong structural control for ascent of hydrothermal fluids and ore accumulation/precipitation. The style of mineralization at the El Romeral is nearly identical to all IOA deposits in the Coastal Cordillera of northern Chile and thus it seems plausible to suggest that the formation of IOA deposits is controlled by extensional forces related to tectonic movements. These structures allowed rapid transport and precipitation at various levels within the deposit. The ore petrology/geochemistry reflects decreasing T and P conditions towards the upper levels in the deposit, and record the transition from magmatic to hydrothermal processes.

Acknowledgments

This work was funded by FONDECYT grant #1140780 to F.Barra and the Millennium Science Initiative (MSI) through Millennium Nucleus for Metal Tracing along Subduction grant NC130065. We are grateful to chief editor Franco Pirajno, and reviewers Cristiana Ciobanu and Patrick Nadoll for their constructive comments and suggestions that helped improve this manuscript. The authors acknowledge the facilities, and the scientific and technical assistance of the Australian Microscopy & Microanalyses Research Facility at the Centre for Microscopy, Characterisation & Analyses, The University of Western Australia, a facility funded by the University, State and Commonwealth Governments. We are grateful to Carlos Garrido, from the Chemistry Department of the Universidad de Chile, for his help with micro-Raman analyses. We thank the Compañía Minera del Pacífico (CAP) and their geology team for their helpful logistical support, and for providing access to the mine and drill core library.

REFERENCES

- Audétat, A., Günther, D., Heinrich, C.A., 2000. Causes for large-scale metal zonation around mineralized plutons: fluid inclusion LA-ICP-MS evidence from the Mole Granite, Australia. *Econ. Geol.*, 95, 1563-1581. <https://doi.org/10.2113/gsecongeo.95.8.1563>
- Bajwah, Z.U., Secombe, P.K., Offler, R., 1987. Trace element distribution, Co:Ni ratios and genesis of the Big Cadia iron-ore deposit, New South Wales, Australia. *Miner. Deposita* 22, 292–300. <https://doi.org/10.1007/bf00204522>
- Bao, B., Webster, J.D., Zhang, D., Goldoff, B.A., Zhang, R., 2016. Compositions of biotite, amphibole, apatite and silicate melt inclusions from the Tongchang mine, Dexing porphyry deposit, SE China: Implications for the behavior of halogens in this mineralized porphyry system. *Ore Geol. Rev.* 79, 443-462. <https://doi.org/10.1016/j.oregeorev.2016.10.016>
- Barra, F., Reich, M., Selby, D., Rojas, P., Simon, A., Salazar, E., Palma, G., 2017. Unraveling the origin of the Andean IOCG clan: A Re-Os isotope approach. *Ore Geol. Rev.* 81, 62-78. <https://doi.org/10.1016/j.oregeorev.2016.10.016>
- Barth, A.P., Dorais, M.J., 2000. Magmatic anhydrite in granitic rocks: First occurrence and potential petrologic consequences. *Am. Mineral.* 85, 430-435. <https://doi.org/10.2138/am-2000-0404>
- Barton, M.D., 2014, Iron oxide (-Cu-Au-REE-P-Ag-U-Co) systems. *Treatise on Geochemistry* 2nd Edition, 13, 515-541. <http://dx.doi.org/10.1016/B978-0-08-095975-7.01123-2>
- Bau, M., Alexander, B.W., 2009. Distribution of high field strength elements (Y, Zr, REE, Hf, Ta, Th, U) in adjacent magnetite and chert band and in reference standards FeR-3 and FeR-4 from the Temagami iron-formation, Canada, and the redox level of the Neoproterozoic ocean. *Precambrian Res.* 174, 337-346. <https://doi.org/10.1016/j.precamres.2009.08.007>
- Belousova, E.A., Walters, S., Griffin, W.L., O'Reilly, S.Y., 2001. Trace-element signatures of apatites in granitoids from the Mt Isa Inlier, northwestern Queensland. *Austr. J. Earth Sci.* 48, 603-619. <https://doi.org/10.1046/j.1440-0952.2001.00879.x>
- Bilenker, L.D., Simon, A.C., Reich, M., Lundstrom, C.C., Gajos, N., Bindeman, I., Barra, F., Munizaga, R., 2016. Fe-O stable isotope pairs elucidate a high-temperature origin of Chilean iron oxide-apatite deposits. *Geochim. Cosmochim. Acta* 177, 94-104. <https://doi.org/10.1016/j.gca.2016.01.009>
- Boctor, N.Z., Popp, R.K., Frantz, J.D., 1980. Mineral-solution equilibria-IV. Solubilities and the thermodynamic properties of Fe_2O_3^0 in the system $\text{Fe}_2\text{O}_3\text{-H}_2\text{-H}_2\text{O-HCl}$. *Geochim. Cosmochim. Acta* 44, 1509-1518. [https://doi.org/10.1016/0016-7037\(80\)90115-5](https://doi.org/10.1016/0016-7037(80)90115-5)

Bodnar, R.J., Vityk, M.O., 1994. Interpretation of microthermometric data for H₂O-NaCl fluid inclusions. In: Fluid Inclusions in Minerals, Methods and Applications, De Vivo, B., Frezzotti, M.L. (eds). Virginia Tech, Blacksburg, VA, p.117-130.

Bookstrom, A., 1977. The magnetite deposits of El Romeral, Chile. *Econ. Geol.* 72, 1101-1130. <https://doi.org/10.2113/gsecongeo.72.6.1101>

Bralia, A., Sabatini, G., Troja, P., 1979. A re-evaluation of the Co/Ni ratio in pyrite as geochemical tool in ore genesis problems. *Miner. Deposita* 14, 353–374. <https://doi.org/10.1007/bf00206365>

Brown, M., Díaz, F., Grocott, J., 1993. Displacement History of the Atacama Fault System, 25°00'S 27°00'S, Northern Chile. *Geol. Soc. Am. Bull.* 105, 1165-1174. [https://doi.org/10.1130/0016-7606\(1993\)105<1165:dhotaf>2.3.co;2](https://doi.org/10.1130/0016-7606(1993)105<1165:dhotaf>2.3.co;2)

Campbell, F.A, Ethier, V.G., 1984. Nickel and cobalt in pyrrhotite and pyrite from the Faro and Sullivan orebodies. *Can. Mineral.* 22, 503–506.

CAP Minería 2014 Annual Report. http://www.capmineria.cl/wp-content/uploads/2015/03/cap_mineria_memoria_2014.pdf

Charrier, R., Pinto, L., and Rodríguez, M.P., 2007, Tectonostratigraphic evolution of the Andean Orogen in Chile. In: *The Geology of Chile*, Moreno, T., Gibbons, W. (eds.). Geological Society of London, p. 21-114.

Childress, T.M., Simon, A.C., Day, W.C., Lundstrom, C.C., Bindeman, I.N., 2016. Iron and oxygen isotope signatures of the Pea Ridge and Pilot Knob magnetite-apatite deposits, Southeast Missouri, USA. *Econ. Geol.* 111, 2033-2044. <https://doi.org/10.2113/econgeo.111.8.2033>

Chou, I.C., Eugster, H.P., 1977. Solubility of magnetite in supercritical chloride solutions. *Am. J. Sci.* 277, 296-1314. <https://doi.org/10.2475/ajs.277.10.1296>

Coira, B., Davidson, C., Mpodozis, C., Ramos, V., 1982. Tectonic and magmatic evolution of the Andes of northern Argentina and Chile. *Earth Sci. Rev.* 18, 303-332. [https://doi.org/10.1016/0012-8252\(82\)90042-3](https://doi.org/10.1016/0012-8252(82)90042-3)

Cook, N.J., Chryssoulis, S.L., 1990. Concentrations of invisible gold in the common sulfides. *Can. Mineral.* 28, 1–16.

Dare, S.A.S., Barnes, S.-J., Beaudoin, G., Méric, J., Boutroy, E., Potvin-Doucet, C., 2014. Trace elements in magnetite as petrogenetic indicators. *Miner. Deposita* 49, 785–796. <https://doi.org/10.1007/s00126-014-0529-0>

Dare, S.A.S., Barnes, S., Beaudoin, G., 2015. Did the massive magnetite “lava flows” of El Laco (Chile) form by magmatic or hydrothermal processes? New constraints from magnetite

composition by LA-ICP-MS: *Miner. Deposita* 50, 607-617. <https://doi.org/10.1007/s00126-014-0560-1>

Day, W.C., Slack, J.F., Ayuso, R.A., Seeger, C.M., 2016. Regional geologic and petrologic framework for iron oxide \pm apatite \pm rare earth element and iron oxide copper-gold deposits of the Mesoproterozoic St. Francois Mountains Terrane, Southeast Missouri, USA. *Econ. Geol.* 111, 1825-1858. <https://doi.org/10.2113/econgeo.111.8.1825>

Deditius, A., Reich, M., Kesler, S.E., Utsunomiya, S., Chryssoulis, S., Walshe, J.L., Hough, R., Ewing, R.C., 2014. The coupled geochemistry of Au and As in pyrite from hydrothermal ore deposits. *Geochim. Cosmochim. Acta* 140, 644-670. <https://doi.org/10.1016/j.gca.2014.05.045>

De Melo, G.H.C., Monteiro, L.V.S., Xavier, R.P., Moreto, C.P.N., Santiago, E.S.B., Dufrane, S.A., Aires, B., Santos, A.F.F., 2017. Temporal evolution of the giant Salobo IOCG deposit, Carajás Province (Brazil): constraints from paragenesis of hydrothermal alteration and U-Pb geochronology. *Miner. Deposita* 52, 709-732. <https://doi.org/10.1007/s00126-016-0693-5>

Dobbs, M., 1978. Distribución de vanadio y titanio en el Cuerpo Principal de la mina El Romeral. Honours thesis. Universidad de Chile, Facultad de Ciencias Físicas y Matemáticas, Departamento de Geología, Santiago, p.86.

Dupuis, C., Beaudoin, G., 2011. Discriminant diagrams for iron oxide trace element fingerprinting of mineral deposit types. *Miner. Deposita* 46, 319-335. <https://doi.org/10.1007/s00126-011-0334-y>

Emparán, C., Pineda, G., 2000. Área La Serena-La Higuera, Región de Coquimbo. Servicio Nacional de Geología y Minería. Mapas Geológicos, no.18, 1 mapa escala 1:100.000, Santiago.

Emparán, C., Pineda, G., 2005. Geología del Área Andacollo-Puerto Aldea, Región de Coquimbo. Servicio Nacional de Geología y Minería. Carta Geológica de Chile, Serie Geología Básica, no.96, 1:1000.000, Santiago.

Espinoza, L., 2000. Estudio petrográfico del cuerpo Cerro Principal del distrito ferrífero El Romeral IV región- La Serena, Chile. Honours thesis, Universidad de Chile, Facultad de Ciencias Físicas y Matemáticas, Departamento de Geología, Santiago, Chile.

Gualda, G.A.R., Ghiorso, M.S., 2007. Magnetite scavenging and the buoyancy of bubbles in magmas. Part 2: Energetics of crystal-bubble attachment in magmas. *Contrib. Mineral. Petr.* 154, 479-490. <https://doi.org/10.1007/s00410-007-0206-8>

Heinrich, C.A., Ryan, C.G., Mernagh, T.P., Eadington, P.J., 1992. Segregation of ore metals between magmatic brine and vapor. *Econ. Geol.* 87, 1566-1583. <https://doi.org/10.2113/gsecongeo.87.6.1566>

Henry, D.J., Guidotti, C.V., Thomson, J.A., 2005. Ti-saturation surface for low-to-medium pressure metapelitic biotites: Implications for geothermometry and Ti-substitution mechanisms. *Am. Mineral.* 90, 316-328. <https://doi.org/10.2138/am.2005.1498>

Huberty, J.M., Konishi, H., Heck, P.R., Fournelle, J.H., Valley, J.W., Xu, H., 2012. Silician magnetite from the Dales Gorge Member of the Brockman Iron Formations, Hamersley Group, Western Australia. *Am. Mineral.* 97, 26-37. <https://doi.org/10.2138/am.2012.3864>

Hummel, W., Berner, U., Curti, E., Pearson, F.J., Thoenen, T., 2002. Nagra/PSI chemical Thermodynamic Data Base 01/01. Nagra NTB 02-16, Nagra, Wettingen, Switzerland.

Hurwitz, S., Navon, O., 1994. Bubble nucleation in rhyolitic melts: Experiments at high pressure, temperature, and water content. *Earth Planet. Sci. Lett.* 122, 267-280. [https://doi.org/10.1016/0012-821x\(94\)90001-9](https://doi.org/10.1016/0012-821x(94)90001-9)

Huston, D.L., Sie, S.H., Suter, G.F., Cooke, D.R., Both, R.A., 1995. Trace elements in sulfide minerals from eastern Australian volcanic-hosted massive sulfide deposits: Part I. Proton microprobe analyses of pyrite, chalcopyrite, and sphalerite, and Part II. Selenium levels in pyrite: Comparison with $\delta^{34}\text{S}$ values and implications for the source of sulfur in volcanogenic hydrothermal systems. *Econ. Geol.* 90, 1167-1196. <https://doi.org/10.2113/gsecongeo.90.5.1167>

Jaillard, E., Soler, P., Carlier, G., Mourier, T., 1990. Geodynamic evolution of the northern and central Andes during early to middle Mesozoic times: a Tethyan model. *J. Geol. Soc.* 147, 1009-1022. <https://doi.org/10.1144/gsjgs.147.6.1009>

James, B.R., 2003. Chromium: Encyclopedia of Water Science. In: Stewart, B.A., Howell, T.A., (eds). Marcel Dekker Inc., p.77-82.

Jenkins, D.M., 1983. Stability and composition relations of calcic amphiboles in ultramafic rocks. *Contrib. Mineral. Petr.* 83, 375-384. <https://doi.org/10.1007/bf00371206>

Johnson, J.W., Oelkers, E.H., Helgeson, H.C., 1992. SUPCRT92: A software package for calculating the standard molal thermodynamic properties of minerals, gases, aqueous species, and reactions from 1 to 5000 bar and 0 to 1000°C. *Comput. Geos.* 18, 899-947. [https://doi.org/10.1016/0098-3004\(92\)90029-q](https://doi.org/10.1016/0098-3004(92)90029-q)

Jonsson, E., Troll, V.R., Högdahl, K., Harris, C., Weis, F., Nilsson, K.P., Skelton, A., 2013. Magmatic origin of giant 'Kiruna-type' apatite-iron-oxide ores in Central Sweden. *Sci. Rep.* 3. <https://doi.org/10.1038/srep01644>

Knipping J.L., Bilenker, L.D., Simon, A.C., Reich, M., Barra, F., Deditius, A.P., Lundstrom, C., Bindeman, I., Munizaga, R., 2015a. Giant Kiruna-type deposits form by efficient flotation of magmatic magnetite suspensions. *Geology*, 43, 591-594. <https://doi.org/10.1130/g36650.1>

Knipping J.L., Bilenker, L.D., Simon, A.C., Reich, M., Barra, F., Deditius, A.P., Wälle, M., Heinrich, C.A., Holtz, F., Munizaga, R., 2015b. Trace elements in magnetite from massive iron oxide-apatite deposits indicate a combined formation by igneous and magmatic-hydrothermal processes. *Geochim. Cosmochim. Acta* 171, 15-38. <https://doi.org/10.1016/j.gca.2015.08.010>

Koglin, N., Frimmel, H.E., Minter, W.E.L., Brätz, H., 2010. Trace-element characteristics of different pyrite types in Mesoarchaeon to Palaeoproterozoic placer deposits. *Miner. Deposita* 45, 259–280. <https://doi.org/10.1007/s00126-009-0272-0>

Krneta, S., Ciobanu, C.L., Cook, N.J., Ehrig, K., Kontonikas-Charos, A., 2016. Apatite at Olympic Dam, South Australia: A petrogenetic tool. *Lithos* 262, 470-485. <https://doi.org/10.1016/j.lithos.2016.07.033>

Kulik, D.A., Wagner, T., Dmytrieva, S.V., Kosakowski, G., Hingerl, F.F., Chudnenko, K.V., Berner U., 2013. GEM-Selektor geochemical modeling package: revised algorithm and GEMS3K numerical kernel for coupled simulation codes. *Comp. Geosc.* 17, 1-24. <https://doi.org/10.1007/s10596-012-9310-6>

Kusebauch, C., John, T., Whitehouse, M.J., Klemme, S., Putnis, A., 2015. Distribution of halogens between fluid and apatite during fluid-mediated replacement processes. *Geochim. Cosmochim. Acta* 170, 225-246. <https://doi.org/10.1016/j.gca.2015.08.023>

Laetsch, T., Downs, T., 2006. Software for identification and refinement of cell parameters from powder diffraction data of minerals using the RRUFF project and American Mineralogist Crystal Structure databases. Abstracts from the 19th General Meeting of the International Mineralogical Association, Kobe, Japan, 23-28 July, 2006.

Large, R.R., Danyushevsky, L., Hollit, C., Maslennikov, V., Meffre, S., Gilbert, S., Bull, S., Scott, R., Emsbo, P., Thomas, H., Singh, B., Foster, J., 2009. Gold and trace element zonation in pyrite using a laser imaging technique: Implications for the timing of gold in orogenic and Carlin-style sediment-hosted deposits. *Econ. Geol.* 104, 635–668. <https://doi.org/10.2113/gsecongeo.104.5.635>

Lledo, H.L., Jenkins, D.M., 2008. Experimental Investigation of the Upper Thermal Stability of Mg-rich Actinolite; Implications for Kiruna-Type Iron Deposits. *J. Petrol.* 49, 225-238. <https://doi.org/10.1093/petrology/egm078>

Loberg, E.H., Horndahl, A.-K., 1983. Ferride geochemistry of Swedish Precambrian iron ores. *Miner. Deposita* 18, 487–504. <https://doi.org/10.1007/bf00204493>

Loftus-Hills, G., Solomon, M., 1967. Cobalt, nickel and selenium in sulphides as indicators of ore genesis. *Miner. Deposita* 2, 228–242. <https://doi.org/10.1007/bf00201918>

Maksaev, V., Gardeweg, M., Ramírez, C.F., Zentilli, M., 1988. Aplicación de método de trazas de fisión a la datación de cuerpo de magnetita de El Laco e Incahuasi en el Altiplano de la Región de Antofagasta. Abstract V Congreso Geológico Chileno, Actas 1, B1-B23.

Marks, M.A.W., Wenzel, T., Whitehouse, M.J., Loose, M., Zack, T., Barth, M., Worgard, L., Krasz, V., Eby, N., Stosnach, H., Marki, G., 2012. The volatile inventory (F, Cl, Br, S, C) of magmatic apatite: An integrated analytical approach. *Chem. Geol.* 291, 241-255. <https://doi.org/10.1016/j.chemgeo.2011.10.026>

Ménard, J.J., 1995. Relationship between altered pyroxene diorite and the magnetite mineralization in the Chilean Iron Belt, with emphasis on the El Algarrobo iron deposits (Atacama region, Chile). *Miner. Deposita* 30, 268-274. <https://doi.org/10.1007/bf00196362>

Mookherjee, A., Philip, R., 1979. Distribution of copper, cobalt and nickel in ores and host-rocks, Ingaldhal, Karnataka, India. *Miner. Deposita* 14, 33-55. <https://doi.org/10.1007/bf00201866>

Munoz, J.L., 1992. Calculation of HF and HCl fugacities from biotite compositions: revised equations. *Geol. Soc. Am., Abstract Programs* 24, A221.

Nadoll, P., 2013. Mineral Inclusions in magnetite as a guide to exploration-Preliminary results. *Abstract 12th SGA Biennial Meeting 2013 Proceedings* 1, 280-282.

Nadoll, P., Koenig, A.E., 2011. LA-ICP-MS of magnetite: methods and reference materials. *J. Anal. Atom. Spectrom.* 26, 1872-1877. <https://doi.org/10.1039/c1ja10105f>

Nadoll, P., Mauk, J., Hayes, T.S., Koenig, A.E., Box, S.E., 2012. Geochemistry of magnetite from hydrothermal ore deposits and host rocks of the Mesoproterozoic Belt Supergroup, United States. *Econ. Geol.* 107, 1275-1292. <https://doi.org/10.2113/econgeo.107.6.1275>

Nadoll, P., Angerer, T., Mauk, J.L., French, D., Walshe, J., 2014a. The chemistry of hydrothermal magnetite: a review. *Ore Geol. Rev.* 61, 1-32. <https://doi.org/10.1016/j.oregeorev.2013.12.013>

Nadoll, P., Mauk, J.L., Richard, A.L., Koenig, A.E., 2014b. Geochemistry of magnetite from porphyry Cu and skarn deposits in the southwestern United States. *Miner. Deposita*. <https://doi.org/10.1007/s00126-014-0539-y>

Naranjo, J.A., Henríquez, F., Nyström, J.O., 2010. Subvolcanic contact metasomatism at El Laco Volcanic complex, Central Andes. *Andean Geol.* 37, 110-120. <https://doi.org/10.4067/s0718-71062010000100005>

Nash, W.P., 1984. Phosphate minerals in terrestrial igneous and metamorphic rocks. In: *Phosphate Minerals*, Nriagu, J.O., Moore, P.B. (eds.). Springer-Verlag, New York, p. 215-241. https://doi.org/10.1007/978-3-642-61736-2_6

Naslund, H.R., Henríquez, F., Nyström, J.O., Vivallo, W., Dobbs, F.M., 2002. Magmatic iron ores and associated mineralization: Examples from the Chilean high Andes and

Coastal Cordillera. In: *Hydrothermal Iron Oxide Copper-Gold & Related Deposits: A Global Perspective*, Porter, T.M. (ed.). PGC Publishing, Adelaide 2, 207-226.

Newberry, N.G., Peacor, D.R., Essene, E.J., Geissman, J.W., 1982. Silicon in magnetite: high resolution microanalysis of magnetite-ilmenite intergrowths. *Contrib. Mineral. Petr.* 80, 334–340. <https://doi.org/10.1007/bf00378006>

Nold, J.L., Dudley, M.A. Davidson, P., 2014. The southeast Missouri (USA) Proterozoic iron metallogenic province-Types of deposits and genetic relationships to magnetite-apatite and iron oxide-copper-gold deposits. *Ore Geol. Rev.* 57, 154-171. <https://doi.org/10.1016/j.oregeorev.2013.10.002>

Nyström, J.O., Henríquez, F., 1994. Magmatic features of iron ores of the Kiruna type in Chile and Sweden: Ore textures and magnetite geochemistry. *Econ. Geol.* 89, 820-839. <https://doi.org/10.2113/gsecongeo.90.2.473>

Pacevski, A., Libowitzky, E., Zivkovic, P., Dimitrijevic, R., Cvetkovic, L., 2008. Copper-bearing pyrite from the Coka Marin polymetallic deposit, Serbia: mineral inclusions or true solid solution? *Can. Mineral.* 46, 249-261. <https://doi.org/10.3749/canmin.46.1.249>

Patiño-Douce, A.E., Roden, M.F., Chaumba, F., Fleisher, C., Yogodzinsky, G., 2011. Compositional variability of terrestrial mantle apatites, thermodynamic modeling of apatite volatile contents, and the halogen and water budgets of planetary mantles. *Chem. Geol.* 288, 14-31. <https://doi.org/10.1016/j.chemgeo.2011.05.018>

Piccoli, P., Candela, P., 1994. Apatite in felsic rocks: A model for the estimation of initial halogen concentrations in the Bishop tuff (Long Valley) and Tuolumne intrusive suite (Sierra Nevada Batholith) magmas. *Am. J. Sci.* 294, 92-135. <https://doi.org/10.2475/ajs.294.1.92>

Piña, R., Gervilla, F., Barnes, S.J., Ortega, L., Lunar, R., 2013. Platinum-group elements-bearing pyrite from the Aguablanca Ni-Cu sulphide deposit (SW Spain): a LA-ICP-MS study. *Eur. J. Mineral.* 25, 241-252. <https://doi.org/10.1127/0935-1221/2013/0025-2290>

Radcliff, D., McSween, H.Y., 1969. Copper zoning in pyrite from Cerro de Pasco, Perú: a discussion. *Am. Mineral.* 55, 527-528.

Reed, M.J., Candela, P.A., Piccoli, P.M., 2000. The distribution of rare earth elements between monzogranitic melt and the aqueous volatile phase in experimental investigations at 800°C and 200 MPa. *Contrib. Mineral. Petr.* 140, 251-262. <https://doi.org/10.1007/s004100000182>

Reich, M., Kesler, S.E., Utsunomiya, S., Palenik, C.S., Chryssoulis, S., Ewing, R.C., 2005. Solubility of gold in arsenian pyrite. *Geochim. Cosmochim. Acta* 69, 2781–2796. <https://doi.org/10.1016/j.gca.2005.01.011>

Reich, M., Deditius, A., Chryssoulis, S., Li, J., Ma, C.Q., Parada, M.A., Barra, F., Mittermayr, F., 2013. Pyrite as a record of hydrothermal fluid evolution in porphyry copper system: A SIMS/EMPA trace element study. *Geochim. Cosmochim. Acta* 104, 42-62. <https://doi.org/10.1016/j.gca.2012.11.006>

Reich, M., Simon, A.C., Deditius, A., Barra, F., Chryssoulis, S., Lagas, G., Tardani, D., Knipping, J., Bilenker, L., Sánchez-Alfaro, P., Roberts, M.P., Munizaga, R., 2016. Trace element signature of pyrite from the Los Colorador Iron oxide-apatite (IOA) deposit, Chile: a missing link between Andean IOA and Iron oxide copper-gold systems. *Econ. Geol.* 111, 743-761. <https://doi.org/10.2113/econgeo.111.3.743>

Rhodes, A.L., Oreskes, N., 1999. Oxygen Isotope composition of magnetite deposits at El Laco, Chile: Evidence of formation from isotopically heavy fluids. In: *Geology and Ore Deposits of the Central Andes*, Society of Economic Geologists, Skinner, B.J. (ed.). Special Publication 7, 333-351.

Rhodes, A.L., Oreskes, N., Sheets, S., 1999. Geology and rare earth element geochemistry of magnetite deposits at El Laco, Chile. In: *Geology and Ore Deposits of the Central Andes*, Society of Economic Geologists, Skinner, B.J. (ed.). Special Publication 7, 299-332.

Rojas, P., 2017. Genesis of the El romeral iron ore: New contributions to the understanding of iron-oxide apatite deposits. MSc thesis, Department of Geology, Universidad de Chile, 160 p.

Romer, R.L., Martinsson, O., Perdahl, J.A., 1994. Geochronology of the Kiruna Iron Ores and Hydrothermal Alterations. *Econ. Geol.* 89, 1249-1264. <https://doi.org/10.2113/gsecongeo.89.6.1249>

Rusk, B., Oliver, N., Cleverley, J., Blenkinsop, T., Zhang, D., Williams, P., Habermann, P., 2010. Physical and chemical characteristics of the Ernest Henry iron oxide copper gold deposit, Australia; implications for IOCG genesis. In: *Hydrothermal Iron Oxide Copper-Gold & Related Deposits: a global perspective-advances in the understanding of IOCG deposits*. Porter, T.M. (ed.). Global Perspective Series, Australia 3, 201-218.

Scher, S., Williams-Jones, A.E., Williams-Jones, G., 2013. Fumarolic activity, acid-sulfate alteration, and high sulfidation epithermal precious metal mineralization in the crater of Kawah Ijen Volcano, Java, Indonesia. *Econ. Geol.* 108, 1099-1118. <https://doi.org/10.2113/econgeo.108.5.1099>

Scheuber, E., Bogdanic, T., Jensen, A., Reutter, K.J., 1994. Tectonic development of the North Chilean Andes in relation to plate convergence and magmatism since the Jurassic. In: *Tectonics of the Southern Central Andes. Structure and Evolution of an Active Continental Margin*. Reutter, K. J., Scheuber, E., Wigger, P. (eds) Springer, Heidelberg, 121 - 140. https://doi.org/10.1007/978-3-642-77353-2_9

Scott, J.A.J., Humphreys, M.C.S., Mather, T.A., Pyle, D.M., Stock, M.J., 2015. Insights into the behaviour of S, F, and Cl at Santiaguito Volcano Guatemala, from apatite and glass. *Lithos* 232, 375-394. <https://doi.org/10.1016/j.lithos.2015.07.004>

Shinohara, H., 1987. Partition of chlorine compounds in the system silicate melt and hydrothermal solutions. PhD dissertation, Tokyo Institute of Technology, p.192.

Sillitoe, R.H., Burrows, D.R., 2002. New field evidence bearing on the origin of the El Laco magnetite deposit, northern Chile. *Econ. Geol.* 97, 1101-1109. <https://doi.org/10.2113/97.5.1101>

Simon, A.C., Pettke, T., Candela, P.A., Piccoli, P.M., Heinrich, C.H., 2004. Magnetite solubility and iron transport in magmatic-hydrothermal environments. *Geochim. Cosmochim. Acta* 68, 4905-4914. <https://doi.org/10.1016/j.gca.2004.05.033>

Simon, A.C., Pettke, T., Candela, P.A., Piccoli, P.M., 2008. The partitioning behavior of silver in a vapor-brine-rhyolite melt assemblage. *Geochim. Cosmochim. Acta* 72, 1638-1659. <https://doi.org/10.1016/j.gca.2008.01.003>

Simon, A.C., Ripley, E.M., 2011. The role of magmatic sulfur in the formation of ore deposits. In: *Sulfur in Magmas and Melts: Its importance for natural and technical processes*, Behrens, H., Webster, J.D. (eds). *Reviews in Mineralogy and Geochemistry* 73, 513-578. <https://doi.org/10.2138/rmg.2011.73.16>

Soltani Dehnavi, A., Lentz, D.R., McFarlane, C.R.M., 2015. LA-ICPMS analyses of volatile trace elements in massive sulphides and host rocks of selected VMS deposits of the Bathurst mining camp, New Brunswick: methodology and application to exploration. *Geological Survey of Canada Open File* 7853, p.214. <https://doi.org/10.4095/296545>

Sommerauer, J., Katz-Lehnert, K., 1985. A new partial substitution mechanism of $\text{CO}_3^{(2-)}$ / $\text{CO}_3\text{OH}^{(3-)}$ and $\text{SiO}_4^{(4-)}$ for the $\text{PO}_4^{(3-)}$ group in hydroxyapatite from the Kaiserstuhl alkaline complex (SW-Germany). *Contrib. Mineral. Petr.* 91, 360-368. <https://doi.org/10.1007/bf00374692>

Staudigel, H., Schreyer, W., 1977. The Upper Thermal Stability of Clinocllore, $\text{Mg}_5\text{Al}[\text{AlSi}_3\text{O}_{10}](\text{OH})_8$, at 10-35kb PH_2O . *Contrib. Mineral. Petr.* 61, 187-198. <https://doi.org/10.1007/bf00374367>

Stewart, D.C., 1980. A petrographic, chemical, and experimental study of kaersutite occurrences at Dish Hill, California, with implications for volatiles in the upper mantle. PhD dissertation, The Pennsylvania State University, p. 88.

Tornos, F., Velasco, F., Hanchar, J.M., 2016. Iron-rich melts, magmatic magnetite, and superheated hydrothermal systems: The El Laco deposit, Chile. *Geology* 44, 427-430. <https://doi.org/10.1130/g37705.1>

Treloar, P.J., Colley, H., 1996. Variations in F and Cl contents in apatites from magnetite-apatite ores in northern Chile, and their ore-genetic implications. *Mineral. Mag.* 1996, 285-301. <https://doi.org/10.1180/minmag.1996.060.399.04>

Velasco, F., Tornos, F., Hanchar, J.M., 2016. Immiscible iron-and silica-rich melts and magnetite geochemistry at the El Laco volcano (northern Chile): Evidence for a magmatic origin for the magnetite deposits. *Ore Geol. Rev.* 79, 346-366. <https://doi.org/10.1016/j.oregeorev.2016.06.007>

Webster, J.D., 1990. Partitioning of F between H₂O and CO₂ fluids and topaz rhyolite melt: Implications for mineralizing magmatic-hydrothermal fluids in F-rich granitic systems. *Contrib. Mineral. Petr.* 104, 424-438. <https://doi.org/10.1007/bf01575620>

Webster, J.D., Piccoli, P.M., 2015. Magmatic apatite: a powerful, yet deceptive mineral. *Elements* 11, 177–182. <https://doi.org/10.2113/gselements.11.3.177>

Westhues, A., Hanchar, J.M., LeMessurier, M., Whitehouse, M.J., 2017. Evidence for hydrothermal alteration and source regions for the Kiruna iron oxide-apatite ore (northern Sweden) from zircon Hf and O isotopes. *Geology* 45, 571-574. <https://doi.org/10.1130/g38894.1>

Williams, P.J., Barton, M.D., Johnson, D.A., Fontboté, L., De Haller, A., Mark, G., Oliver, N.H.S., Marschik, R., 2005. Iron oxide copper-gold deposits: Geology, space-time distribution, and possible modes of origin. In: *Economic Geology 100th Anniversary Volume*, Hedenquist, J.W., Thompson, J.F.H., Goldfarb, R.J., Richards, J.P. (eds.), 371-405.

Williams-Jones, A.E., Heinrich, C.A., 2005. Vapor transport of metals and the formation of magmatic-hydrothermal ore deposits. *Econ. Geol.* 100, 1287-1312. <https://doi.org/10.2113/100.7.1287>

Zajacz, Z., Halter, W.E., Pettke, T., Guillong, M., 2008. Determination of fluid/melt partition coefficients by LA-ICPMS analysis of co-existing fluid and silicate melt inclusions: Controls on element partitioning. *Geochim. Cosmochim. Acta* 71, 2169-2197. <https://doi.org/10.1016/j.gca.2008.01.034>

Zajacz, Z., Candela, P.A., Piccoli, P.M., Sanchez-Valle, C., 2012. The partitioning of sulfur and chlorine between andesite melts and magmatic volatiles and the exchange coefficients of major cations. *Geochim. Cosmochim. Acta* 89, 81-101. <https://doi.org/10.1016/j.gca.2012.04.039>

Zhu C., Sverjensky, D.A., 1991. Partitioning of F-Cl-OH between minerals and hydrothermal fluid. *Geochim. Cosmochim. Acta* 55, 1837–1858. [https://doi.org/10.1016/0016-7037\(91\)90028-4](https://doi.org/10.1016/0016-7037(91)90028-4)

Figure Captions

Fig. 1. Map showing the location of major iron oxide-apatite (IOA) and iron oxide-copper-gold (IOCG) deposits from the Cretaceous Chilean Iron Belt along the Atacama Fault System. Modified from Barra et al. (2017).

Fig. 2. Geological map of the El Romeral district showing major units and the main iron ore bodies. Location of the five drill cores studied is also shown (Modified from Rojas, 2017).

Fig. 3. Paragenetic sequence of the main mineralization events conforming the iron ore bodies from El Romeral deposit.

Fig. 4. Back-scattered electron images of magnetite textures. **A.** Inclusion-rich magnetite (Type I) surrounded by inclusion-poor magnetite (Type II). Sample collected from the massive orebody at 347 m depth. **B.** Type III Magnetite with distinct zonation; sample collected from the massive ore body at a 139 m depth. **C.** Type I Magnetite with mineral inclusions aligned along crystallographic planes in magnetite. **D.** Zoned magnetite with abundant nano-inclusions. **E-F.** Disseminated (primary) magnetite with ilmenite exsolutions following crystallographic planes. Mgt: magnetite, Ilm: ilmenite, Qtz: quartz, Nano-incl: nano-inclusions

Fig. 5. EDX elemental map of a representative mineral inclusion hosted in magnetite (Type I) from the massive dike orebody. This composite inclusion contains chlorite with minor Na content, and titanite. Chl: chlorite, Ttn: titanite.

Fig. 6. Back-scattered electron images of mineral inclusions in Type I magnetite: **A.** polycrystalline inclusion with titanite, rutile and chlorite. **B.** Euhedral oriented quartz inclusions, following crystallographic planes. Chl: chlorite, Rt: rutile, Ttn: titanite.

Fig. 7. Representative micro-Raman spectra for **A.** clinocllore, **B.** Ti-pargasite and **C.** quartz inclusions from Type I magnetite. The characteristic peaks for magnetite (black) correspond to the background signal, whereas spectra for standard minerals are shown in blue. Analyzed inclusions spectra are shown in red.

Fig. 8. Elemental WDS maps for a representative sample from massive magnetite ore body. Note high Si, Al, Mg, and Ca content, and minor Ti concentration in inclusion-rich magnetite (Type I), contrasting with inclusion-poor rims (Type II magnetite). Vanadium content is high and generally homogeneous for both magnetite types. Color bars indicate element concentration in wt.%. Mgt: magnetite

Fig. 9. Elemental WDS maps for Type III magnetite showing a distinct Si, Al, Mg, Ti and Fe zonation, and less evident Na zoning.

Fig. 10. Back-scattered electron images of pyrite from two different events of mineralization: **A.** Post-magnetite anhedral pyrite with chalcopyrite inclusions. **B.** Syn-mineralization pyrite surrounded by Type II inclusion-free magnetite. Ccp: chalcopyrite, Mgt: magnetite, Py: pyrite.

Fig. 11. Back-scattered electron images of gangue minerals from two different mineralization events: **A.** First syn-ore event, with actinolite, pyroxene and quartz within Type II magnetite, and **B.** Second syn-ore event characterized by the presence of large actinolite crystals intergrown with massive iron ore. Act: actinolite, Mgt: magnetite, Px: pyroxene, Qtz: quartz.

Fig. 12. Back-scattered electron images of apatite grains. **A.** F-apatite (sample 042; depth 300 m) **B.** OH-apatite with silicate and pyrite inclusions and in contact with a large pyrite grain (sample 147; depth 50 m). Ap: apatite, Py: pyrite.

Fig. 13. Al+Mn vs. Ti+V discrimination diagram proposed by Dupuis and Beaudoin (2011) and modified by Nadoll et al. (2014a). Chemical compositions of magnetite cores from the massive ore body and from disseminated grains (Type I magnetite), and inclusion-poor magnetite observed at Type I magnetite rims (Type II magnetite) are plotted. Mostly all samples plot in and below the Kiruna-type field, with some exception for Type I magnetite with Ti or Al-rich mineral inclusions. Also shown is the compositional trend reported by Knipping et al. (2015a, b) for Los Colorados (LC) magnetite grains (light blue arrow), which shows decreasing Ti+V (wt.%) and Al+Mn (wt.%) contents from cores (Type I magnetite) to rims (Type III magnetite), magnetite types described in LC and that are similar to Types I and II magnetite from El Romeral, respectively.

Fig. 14. Ti vs V concentration plot after Nadoll et al. (2014b) with igneous and hydrothermal fields proposed by Knipping et al. (2015b). Vanadium is relatively constant in El Romeral magnetite, but high Ti concentrations are found in inclusion-rich (Type I) magnetite cores and lower Ti values for inclusion-free (Type II) magnetite rims.

Fig. 15. Discriminant diagram with concentrations of Cr vs V (Knipping et al., 2015b). El Romeral magnetite analyses plot in the Kiruna-type field (Cr<1000 ppm and V>500 ppm). The horizontal red line indicates the EMPA analytical detection limit for Cr. Data source for Kiruna type from Loberg and Horndahl (1983), Nystrom and Henríquez (1994), Dupuis and Beaudoin (2011), Dare et al. (2015).

Fig. 16. Compositional trends obtained by electron microprobe analysis of primary actinolite crystals (Actinolite I) within magnetite (Type II) and later pegmatitic actinolite (Actinolite II) intergrown with massive iron ore. Two different trends are defined: (i) a first trend with Ca- and Mg-rich cores and Fe-rich and Ca-poor rims, similar to the trend reported by Lledo and Jenkins (2008), and (ii) a second trend with Ca-poor cores and Ca-rich rims for Mg-rich pegmatitic actinolite crystals.

Fig. 17. Ternary compositional diagram of Z-site species in apatite, which shows the different apatite types recognized in the El Romeral, i.e., a deep F-rich apatite and a shallow OH-apatite. Apatite compositions for igneous, hydrothermal and sedimentary deposits are also plotted, as well as halogens analysis on apatite from two Chilean IOA deposits (Carmen and Fresia). See text for discussion. Source of data: ¹Webster and Piccoli (2015); ²Treloar and Colley (1996); ³Barth and Dorais (2000), Belousova et al. (2001), Krneta et al. (2016); ⁴Marks et al. (2012), Douce et al. (2011); ⁵Bao et al. (2016).

Fig. 18. Plots of Co and Ni vs Fe concentration. **A.** Cobalt and Fe show a negative correspondence. **B.** Nickel and Fe contents have a random distribution. See text for discussion.

Fig. 19. Co vs Ni correlation diagram showing chemical analysis of pyrite from the El Romeral deposit. Most samples have Co:Ni>0.5, with the highest Co content (2.24 wt.%) found in a pyrite crystal associated with the Type II magnetite (Early Pyrite event). Lower Co values (Co:Ni<0.5) are generally associated with disseminated pyrite in host rocks or to a final event of sulfide mineralization at shallow levels (Late Pyrite event). Plot modified from Reich (2016). Source of data: ¹Lorca (1990), ²Reich (2016), ³Piña et al. (2013), ⁴Rusk et al. (2010), ⁵Soltani et al. (2014), ⁶Reich et al. (2013), ⁷Scher et al. (2013).

Fig. 20. Log of fugacity ratios vs T [K] plots from a hydrothermal fluid in equilibrium with biotite from a late event associated with degassing of a post-ore intrusive body. **A.** $\log (f_{\text{HF}}/f_{\text{HCl}})$ vs T data shows a positive trend and negative fugacity ratios, which reflects the low f_{HF} compared to f_{HCl} **B.** $\log (f_{\text{H}_2\text{O}}/f_{\text{HCl}})$ vs T graphic presents an inverse pattern, as **B.** $\log (f_{\text{H}_2\text{O}}/f_{\text{HF}})$ vs T diagram which shows lower fugacity values with increasing temperature.

Fig. 21. Molality of FeCl_2 vs T[°C] plots obtained by geochemical modeling. **A.** Iron solubility as FeCl_2 . The model results indicate that at high pressure (180-200 MPa) FeCl_2 is more soluble at temperatures >500°C, but as pressure drops, FeCl_2 becomes unstable, resulting in the precipitation of magnetite. **B.** Model results indicate that magnetite precipitation is enhanced (higher efficiency) by rapid decompression. Efficiency: $100 * (\text{moles}_{\text{Mgt (final pressure)}} - \text{moles}_{\text{Mgt (initial pressure)}}) / \text{moles}_{\text{Mgt (final pressure)}}$.

Fig. 22. Schematic magmatic-hydrothermal model for the formation of iron oxide-apatite deposits modified from Knipping et al. (2015a). **A.** Inclusion-rich magnetite crystallization from an intermediate composition silicate melt where mineral inclusions are trapped in magnetite structure. **B.** Bubble nucleation on magnetite surface allows crystals to ascend by positive buoyancy force. The hypersaline magmatic fluid transports iron as a chloride complex and scavenges other metals such as Cu and Au as well as S. **C.** Sudden pressure drop due to extensional faults reduces the solubility of Fe causing the precipitation of hydrothermal magnetite over primary magnetite cores (Type I). From this hydrothermal fluid other minerals form, such as pyroxene, actinolite, quartz and sulfides, which can be trapped within magnetite crystals. Additionally, large actinolite crystals (actinolite II) can form simultaneously with Type II magnetite, mainly at the margins of the magnetite ore body. **D.** Final hydrothermal stage (<600°C) is represented by magnetite veinlets crosscutting the main ore body.

Table 1. Magnetite types observed in the El Romeral district.

Magnetite type	Main features
Type I	Inclusion-rich magnetite with high-temperature inclusions (up to 1020°C). Forms the massive ore bodies (~35 modal%). Also present as disseminated grains.
Type II	Inclusion-free magnetite. Usually as an overgrowth around Type I magnetite. Lower temperature event (up to 840°C). Forms the massive ore bodies (~60 modal %). Also present as disseminated grains.
Type III	Inclusion-free, chemically-zoned magnetite. Locally observed at shallow levels in the massive ore bodies (~5 modal%).
Type IV	Magnetite veinlets that crosscut the massive magnetite ore bodies (late event).

Table 2. Representative EMPA analyses for different magnetite grains (Type I and II) from drill cores PRP-0702 and PRP-0733.

Element	Type I Magnetite								Type II Magnetite							
	Massive				Disseminated				Massive				Disseminated			
Si	0.19	0.36	0.07	0.19	0.01	0.01	0.06	0.04	0.01	0.01	0.01	0.02	0.04	0.04	0.20	0.03
Al	0.03	0.21	0.01	0.09	0.01	0.01	B.D.L	B.D.L	0.03	0.04	0.04	0.02	0.02	0.01	0.09	0.01
Na	B.D.L	0.03	0.20	0.19	0.03	0.14	0.15	0.19	0.02	B.D.L	B.D.L	B.D.L	B.D.L	B.D.L	B.D.L	B.D.L
Mg	0.04	0.22	.	0.08	B.D.L	B.D.L	B.D.L	B.D.L	0.02	B.D.L	B.D.L	B.D.L	0.05	0.06	.	B.D.L
Ti	0.03	0.04	0.35	0.14	.	0.01	.	.	0.01	.	.	.	B.D.L	B.D.L	0.07	.
Ca	0.12	0.08	0.08	0.08	0.03	0.15	0.10	0.04	0.01	0.01	0.01	0.01	0.03	0.01	0.04	0.03
K	0.09	0.05	0.02	0.03	0.01	0.01	0.03	0.03	0.01	0.01	.	0.11	0.02	0.02	0.04	0.01
Fe	0.05	0.03	0.03	0.02	B.D.L	B.D.L	B.D.L	B.D.L	B.D.L	B.D.L	B.D.L	B.D.L	0.04	0.04	0.08	0.05
Cr	71.54	71.52	70.17	70.87	0.05	0.03	0.03	0.02	0.04	0.04	0.08	0.05
V	B.D.L	B.D.L	B.D.L	B.D.L	72.08	71.53	71.36	71.26	B.D.L	B.D.L	B.D.L	B.D.L	B.D.L	B.D.L	B.D.L	B.D.L
Mn
O	0.26	0.25	0.26	0.27	0.27	0.28	0.28	0.28	0.26	0.26	0.25	0.24	0.25	0.23	0.24	0.25
Total	0.02	0.02	0.08	0.07	0.01	0.03	0.07	0.06	0.02	0.02	0.02	0.02	0.01	0.01	0.01	0.01
	27.81	28.26	27.38	27.76	27.72	27.65	27.61	27.53	27.80	27.94	27.94	27.75	28.02	27.54	27.74	27.48
	100.1	101.0			100.2				100.4	100.9	100.9	100.2			100.1	
	3	4	98.64	99.75	0	99.85	99.67	99.45	4	3	5	9	99.78	99.10	6	99.98

Note: Detection limits for all elements is 0.01 wt.%, except for Na which is 0.02 wt.%. All concentrations reported in wt.%. Oxygen content is calculated based on ideal formula.

B.D.L: Below detection limit.

Table 3. Statistical parameters for EMPA measurements of Co, Ni, and Cu from pyrite crystals from drill cores PRP-0853 and DDH-5008.

Sample		149-01				149-02				149-04			
		n=4				n=19				n=4			
Elements	D.L.	Mean	1 σ	Min	Max	Mean	1 σ	Min	Max	Mean	1 σ	Min	Max
Cu	0.01	0.26	0.41	0.03	0.87	0.26	0.58	B.D.L	1.56	0.05	0.04	B.D.L	0.08
Ni	0.01	0.03	0.02	0.02	0.05	0.04	0.02	B.D.L	0.07	0.38	0.25	B.D.L	0.56
Co	0.01	0.74	0.32	0.44	1.14	0.16	0.19	0.01	0.62	0.25	0.35	0.02	0.78
Sample		149-06				149-07				149-09			
		n=9				n=3				n=16			
Elements	D.L.	Mean	1 σ	Min	Max	Mean	1 σ	Min	Max	Mean	1 σ	Min	Max
Cu	0.01	B.D.L	-	B.D.L	B.D.L	0.21	0.25	B.D.L	0.39	0.01	0.01	B.D.L	0.02
Ni	0.01	0.35	0.31	0.02	0.76	0.07	0.06	0.03	0.14	0.17	0.11	B.D.L	0.33
Co	0.01	0.05	0.03	B.D.L	0.09	0.13	0.09	0.07	0.24	1.04	0.82	0.02	2.24
Sample		149-10				157-01				157-02			
		n=11				n=2				n=1			
Elements	D.L.	Mean	1 σ	Min	Max	Mean	1 σ	Min	Max	Mean	1 σ	Min	Max
Cu	0.01	0.05	0.04	0.01	0.14	0.01	0	B.D.L	0.01	0.01	0	0.01	0.01
Ni	0.01	0.07	0.02	B.D.L	0.11	0.03	0	B.D.L	0.03	0.33	0	0.33	0.33
Co	0.01	0.05	0.02	0.03	0.09	0.94	0.30	0.73	1.15	0.01	0	0.01	0.01
Sample		157-03				157-04				157-07			
		n=2				n=20				n=1			
Elements	D.L.	Mean	1 σ	Min	Max	Mean	1 σ	Min	Max	Mean	1 σ	Min	Max
Cu	0.01	B.D.L	0	B.D.L	B.D.L	0.01	0.003	B.D.L	0.02	B.D.L	-	B.D.L	B.D.L
Ni	0.01	0.27	0.27	0.04	0.51	0.45	0.12	0.06	0.67	0.61	0	0.61	0.61
Co	0.01	B.D.L	0	B.D.L	B.D.L	0.06	0.11	B.D.L	0.33	0.01	0	0.01	0.01
Sample		133-01				133-02				133-05			
		n=1				n=1				n=2			
Elements	D.L.	Mean	1 σ	Min	Max	Mean	1 σ	Min	Max	Mean	1 σ	Min	Max
Cu	0.01	B.D.L	-	B.D.L	B.D.L	B.D.L	-	B.D.L	B.D.L	0.15	0	0.15	0.15
Ni	0.01	0.04	0	0.04	0.04	0.24	0	0.24	0.24	0.32	0.07	0.28	0.37
Co	0.01	0.10	0	0.10	0.10	0.04	0	0.04	0.04	0.06	0.01	0.05	0.06

Note: Detection limit for Cu, Co, and Ni is 0.01 wt.%. All concentrations reported in wt.%

B.D.L: Below detection limit.

Table 4. Representative EMPA analyses for actinolite crystals (Types I, II, and III) from drill cores PRP-0702, PRP-0733, and DDH-5008.

Element	Actinolite I					Actinolite II					Actinolite III				
F	B.D.L	0.12	B.D.L	0.02	B.D.L	0.14	0.17	0.11	0.11	0.29	0.12	0.14	B.D.L	0.11	0.04
Cl	B.D.L	B.D.L	B.D.L	B.D.L	B.D.L	B.D.L	B.D.L	0.03	0.02	0.02	0.03	0.02	0.03	0.03	0.04
Ca	9.05	9.05	9.30	9.22	9.16	9.47	9.27	8.61	8.52	8.63	8.34	8.35	8.26	8.33	8.53
Si	23.72	23.78	24.50	24.83	24.78	26.10	25.77	25.94	26.10	26.17	24.44	24.11	23.86	24.79	24.61
Mg	8.60	8.62	9.10	9.30	9.07	11.40	10.74	11.39	11.31	11.38	10.36	10.49	10.40	10.96	10.71
Al	1.49	1.35	0.71	0.70	0.76	0.65	0.34	0.37	0.36	0.35	2.12	2.16	2.43	1.95	2.48
Mn	0.10	0.10	0.08	0.09	0.09	B.D.L	0.05	0.05	B.D.L	B.D.L	0.28	0.36	0.37	0.34	0.39
Na	0.19	0.17	0.07	0.07	0.09	0.12	0.04	0.29	0.31	0.28	0.49	0.48	0.54	0.43	0.54
Ti	B.D.L	B.D.L	B.D.L	B.D.L	B.D.L	B.D.L	B.D.L	B.D.L	B.D.L	B.D.L	0.16	0.14	0.13	0.14	0.15
K	0.09	0.07	B.D.L	0.02	B.D.L	B.D.L	0.01	0.05	0.03	0.02	0.03	0.05	0.10	B.D.L	0.10
Cr	B.D.L	B.D.L	B.D.L	B.D.L	B.D.L	B.D.L	B.D.L	B.D.L	B.D.L	B.D.L	B.D.L	B.D.L	B.D.L	B.D.L	B.D.L
Fe	11.29	11.44	10.71	10.28	10.20	6.05	8.10	7.21	7.13	7.04	6.97	7.17	7.79	6.88	7.71
V	0.07	0.08	0.04	0.04	0.05	B.D.L	B.D.L	B.D.L	B.D.L	B.D.L	0.03	B.D.L	0.04	B.D.L	B.D.L
O	42.84	42.83	43.21	43.58	43.38	45.29	44.65	44.90	44.95	45.07	44.13	43.94	44.00	43.67	44.08
H	0.23	0.23	0.23	0.23	0.23	0.24	0.23	0.24	0.24	0.24	0.24	0.24	0.23	0.24	0.35
Total	97.68	97.82	97.95	98.37	97.81	99.46	99.37	99.20	99.08	99.49	97.74	97.67	98.16	97.87	99.72
Fe#	0.36	0.37	0.34	0.32	0.33	0.19	0.25	0.22	0.22	0.21	0.23	0.23	0.25	0.21	0.24

Note: Detection limits for all elements is 0.01 wt.%, except for F, Mn, and Fe which is 0.03 wt.%. All concentrations reported in wt.%. Oxygen and H contents are calculated based on ideal formulas.

B.D.L: Below detection limit.

Table 5. Statistical parameters for halogen contents (formula values) in apatite from drill cores PRP-0702 (~300 m depth for sample 042) and PRP-0853 (~50 m depth for sample 147).

Sample	F-apatite											
	042-01				042-02				042-03			
	n=3				n=2				n=5			
Elements	Mean	1 σ	Min	Max	Mean	1 σ	Min	Max	Mean	1 σ	Min	Max
F Formula	0.45	0.01	0.44	0.47	0.49	0.04	0.46	0.51	0.46	0.01	0.44	0.47
Cl Formula	0.12	0.004	0.12	0.13	0.12	0.02	0.11	0.13	0.11	0.01	0.10	0.12
OH Formula	0.42	0.02	0.41	0.44	0.39	0.02	0.38	0.40	0.43	0.01	0.42	0.44
Sample	OH-apatite											
	147-01				147-02				147-03			
	n=24				n=2				n=2			
Elements	Mean	1 σ	Min	Max	Mean	1 σ	Min	Max	Mean	1 σ	Min	Max
F Formula	0.16	0.01	0.14	0.18	0.16	0.01	0.16	0.16	0.16	0.01	0.16	0.16
Cl Formula	0.21	0.01	0.19	0.24	0.18	0.01	0.17	0.19	0.20	0.01	0.19	0.20
OH Formula	0.62	0.01	0.61	0.65	0.66	0.01	0.65	0.66	0.65	0.01	0.64	0.65
Sample	OH-apatite											
	147-04				147-05							
	n=4				n=4							
Elements	Mean	1 σ	Min	Max	Mean	1 σ	Min	Max				
F Formula	0.16	0.01	0.16	0.17	0.46	0.01	0.44	0.47				
Cl Formula	0.23	0.02	0.20	0.24	0.11	0.01	0.10	0.12				
OH Formula	0.61	0.02	0.60	0.64	0.43	0.01	0.42	0.44				

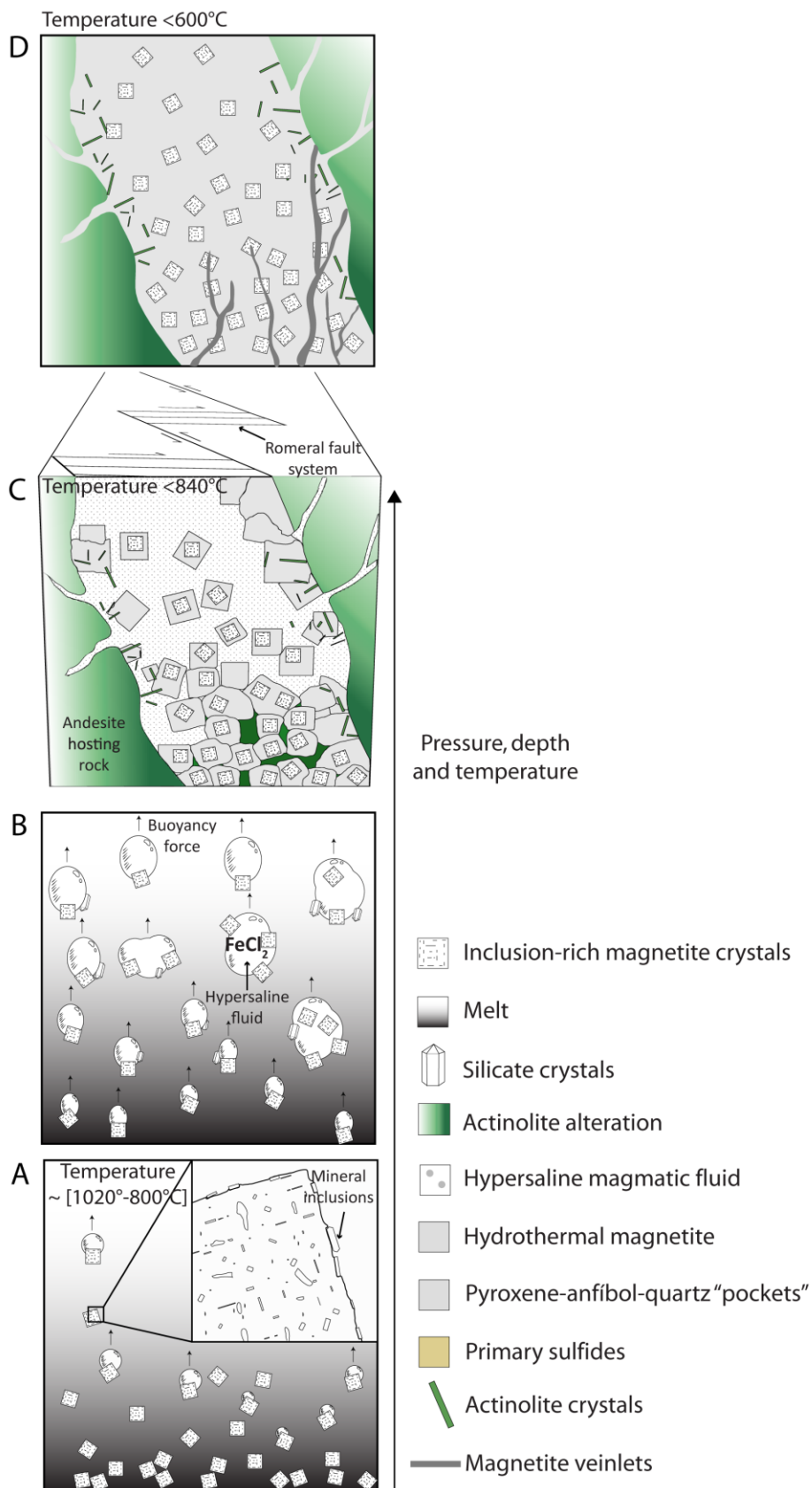
El Romeral magnetite ore was formed by two main mineralization events: a high-temperature magmatic event followed by a second event with magnetite precipitated over primary magmatic magnetite.

This second event is consistent with hydrothermal precipitation of magnetite from a magmatic-hydrothermal fluid with strongly fluctuating composition as a result of decompression and decreasing temperature.

Mineral inclusions in magnetite grains reflect a transition from magmatic to hydrothermal dominated processes in the formation of El Romeral.

The Fe ore in iron oxide-apatite deposits is formed by flotation and coalescence of primary magmatic magnetite-bubble pairs within a magma chamber.

MANUSCRIPT



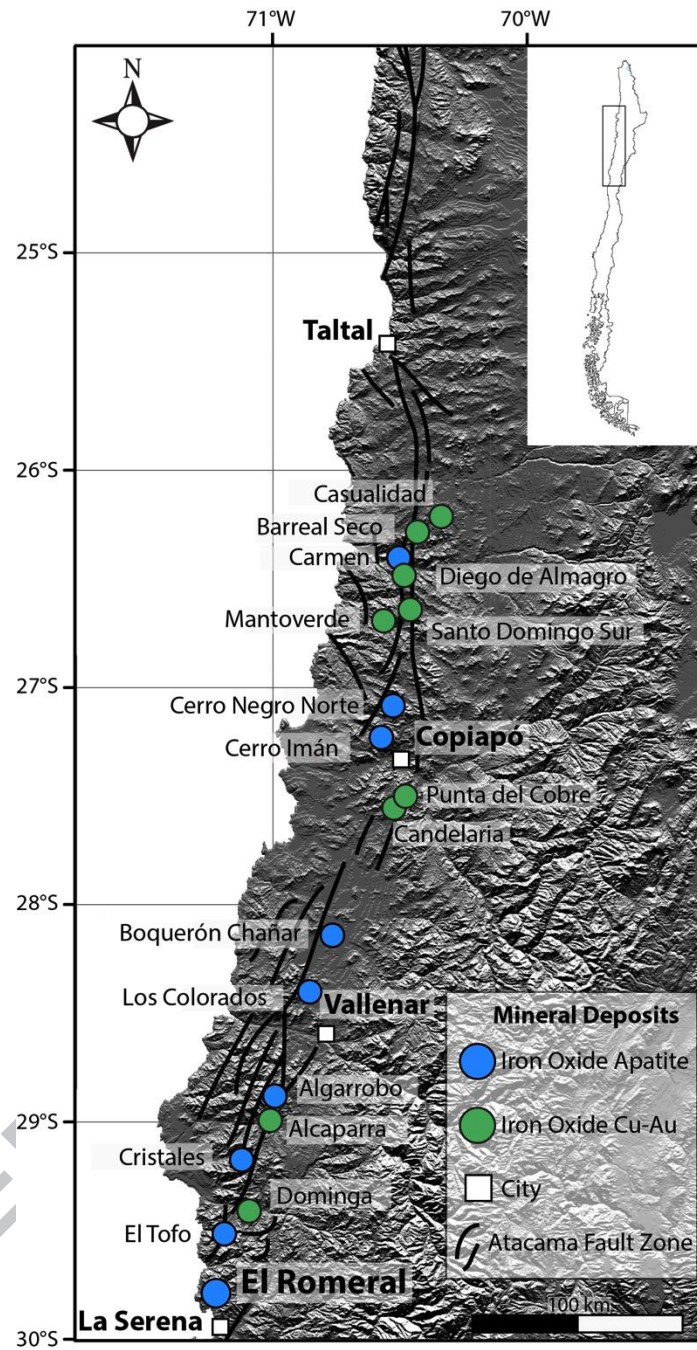


Figure 1

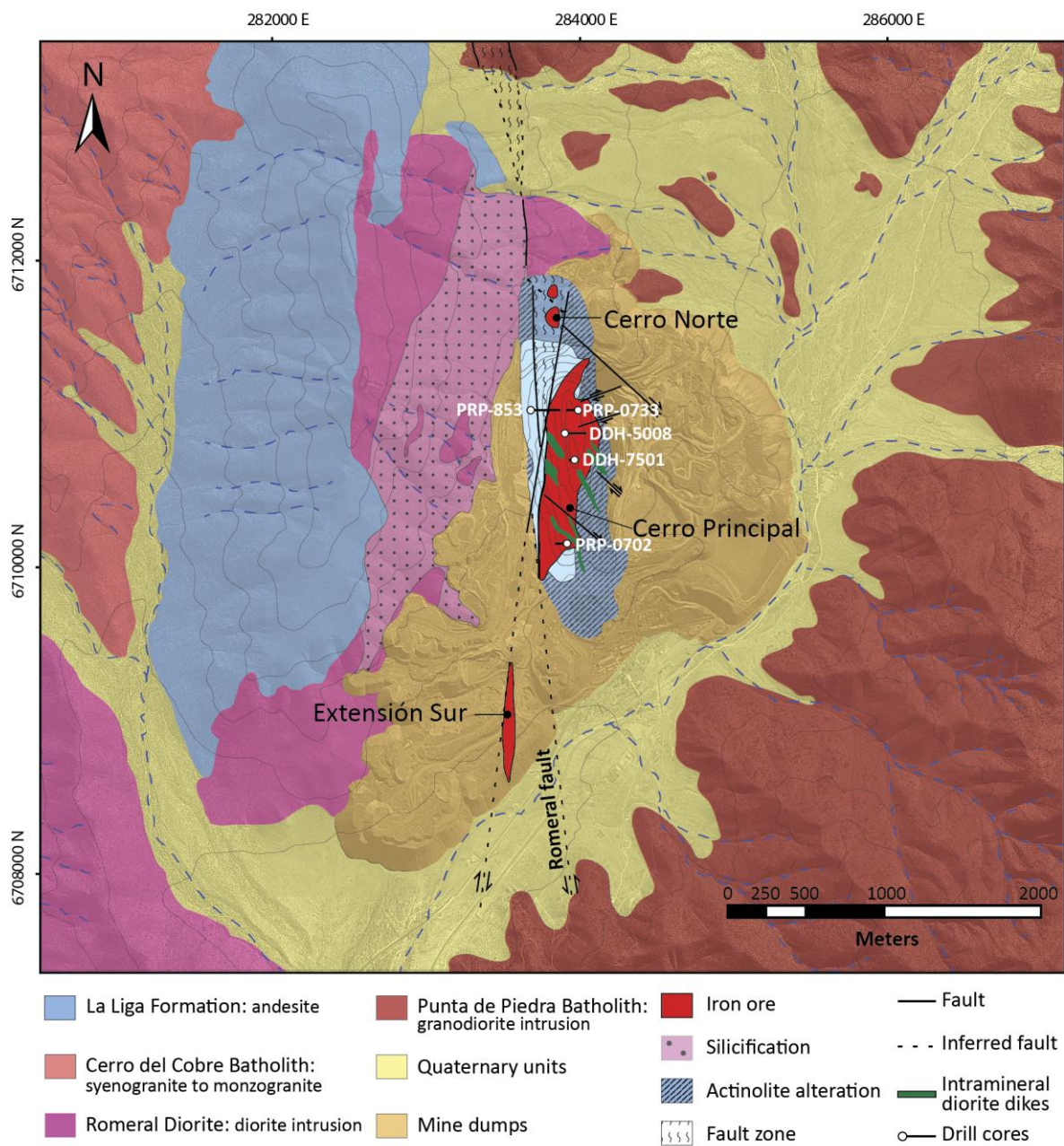


Figure 2



Figure 3

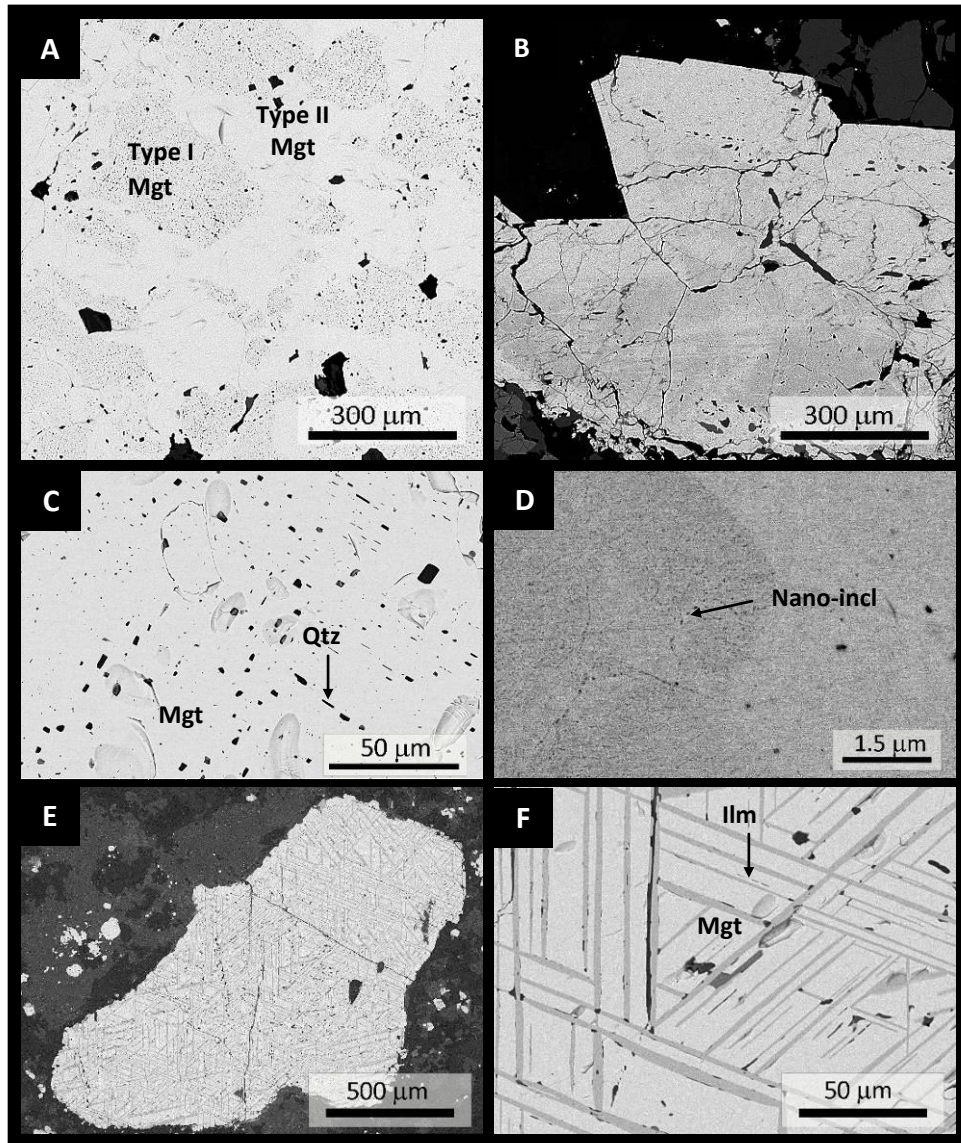


Figure 4

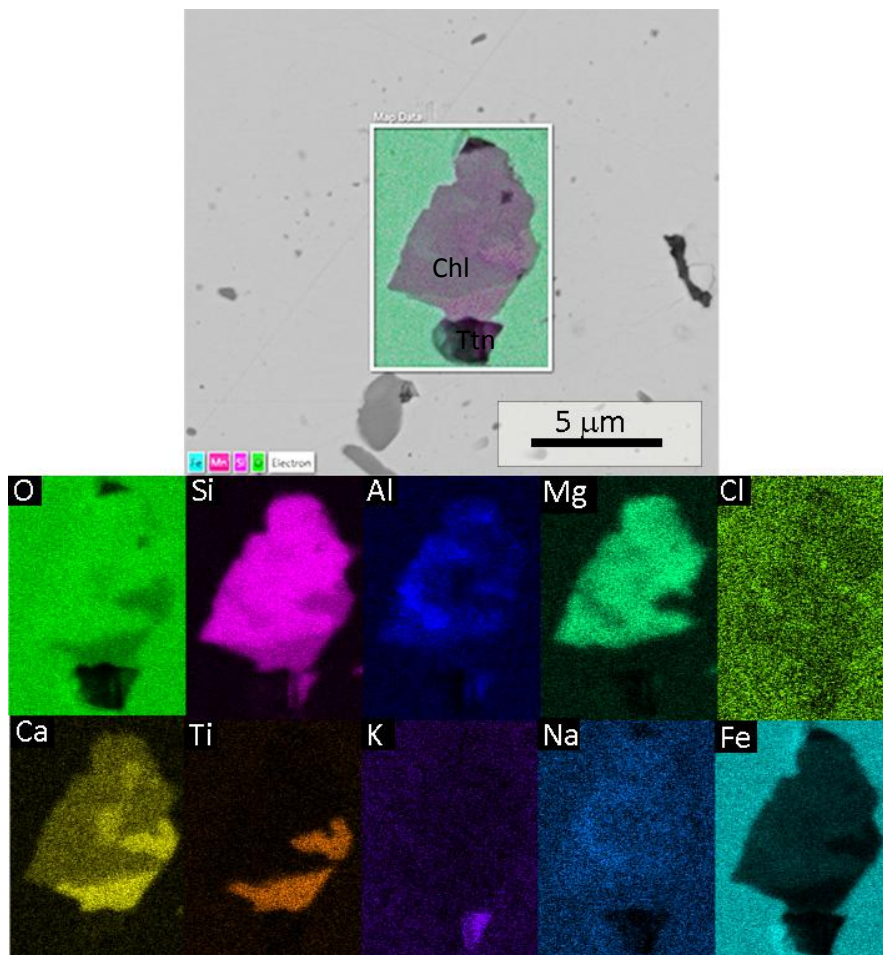


Figure 5

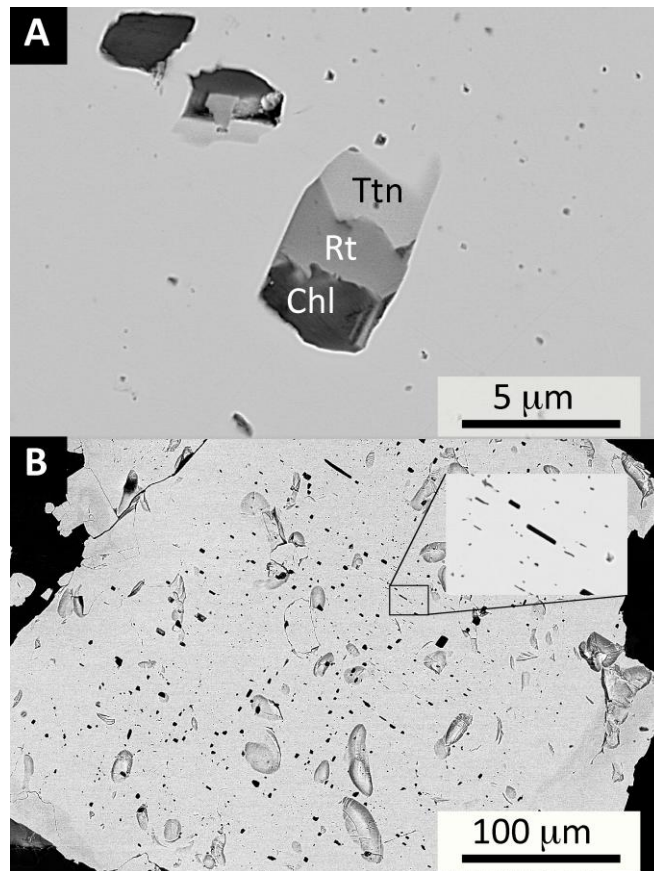


Figure 6

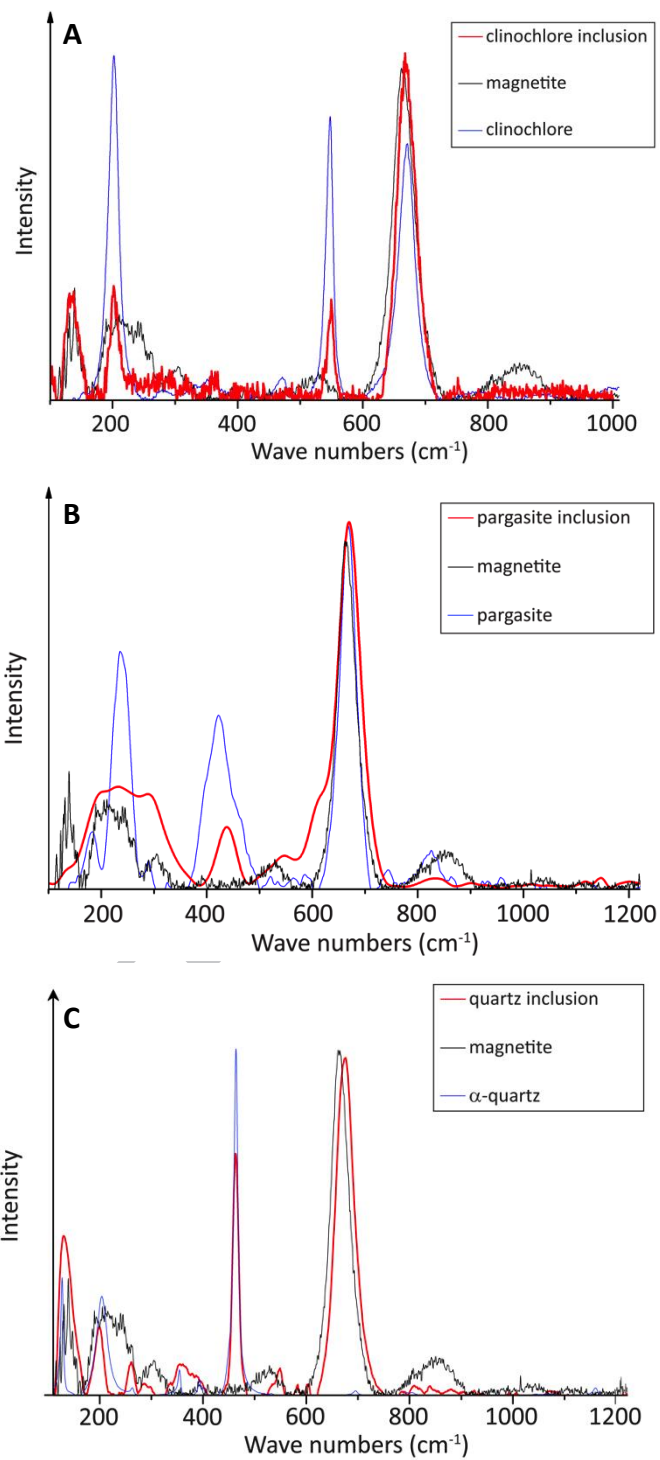


Figure 7

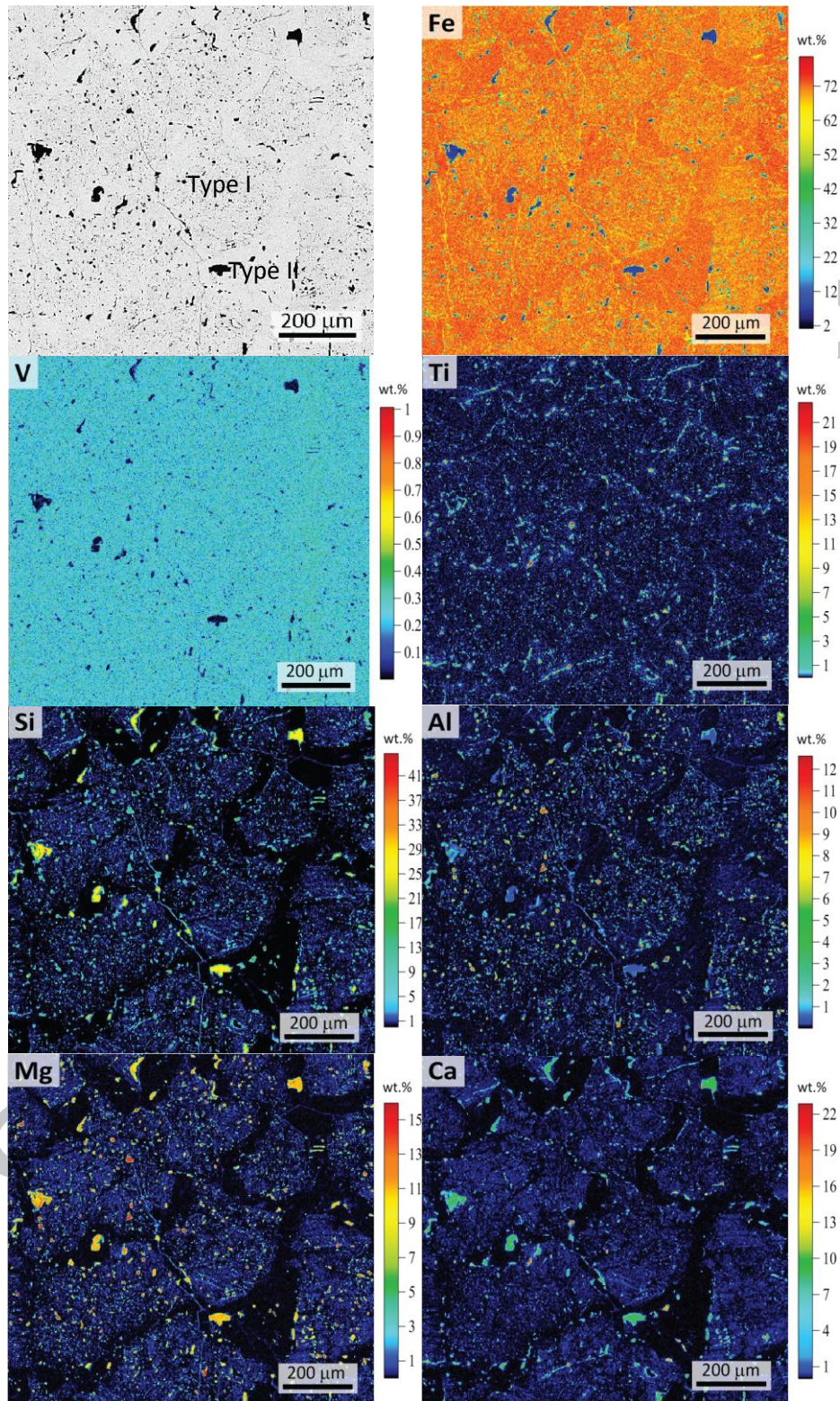


Figure 8

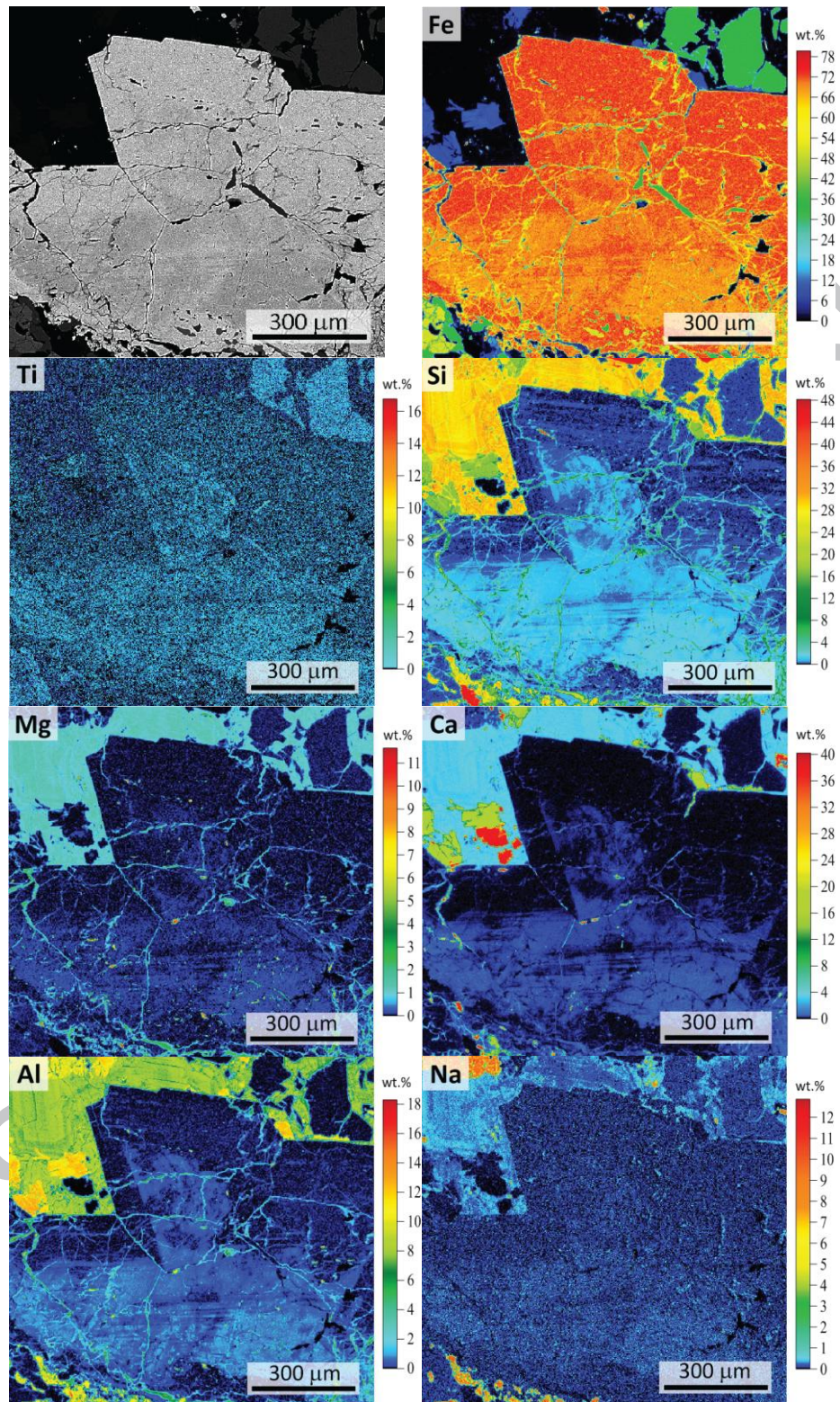


Figure 9

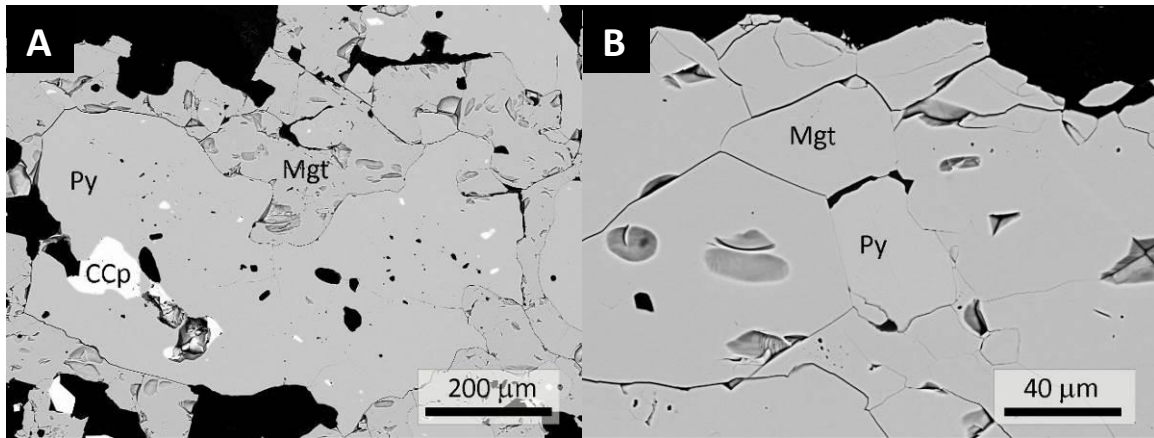


Figure 10

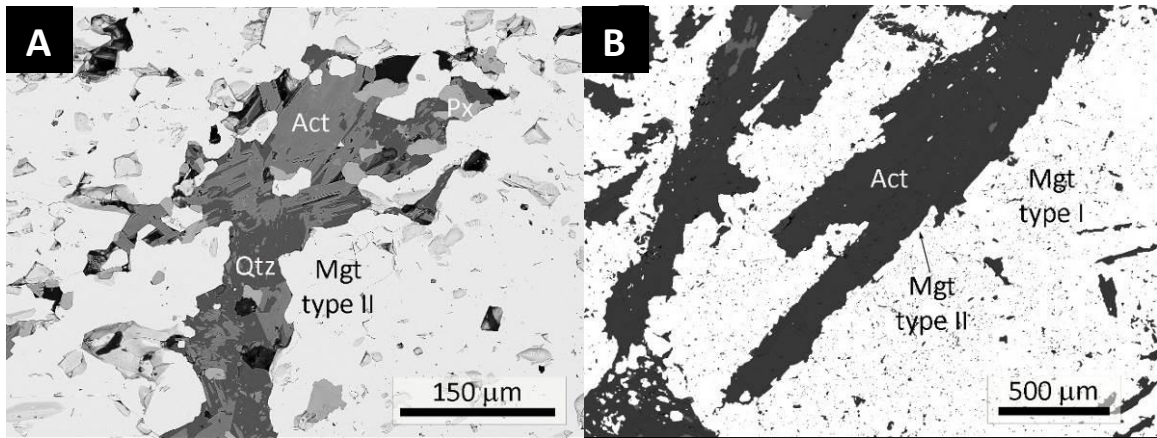


Figure 11

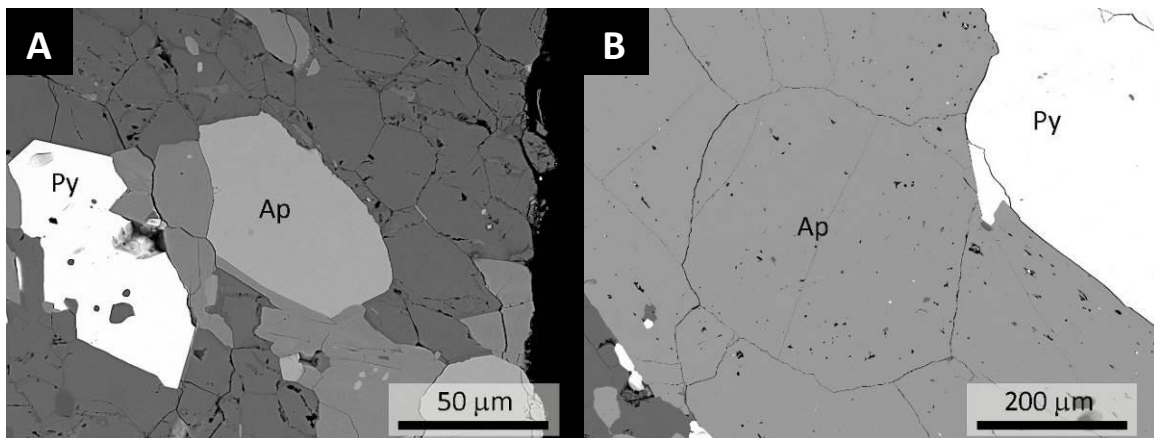


Figure 12

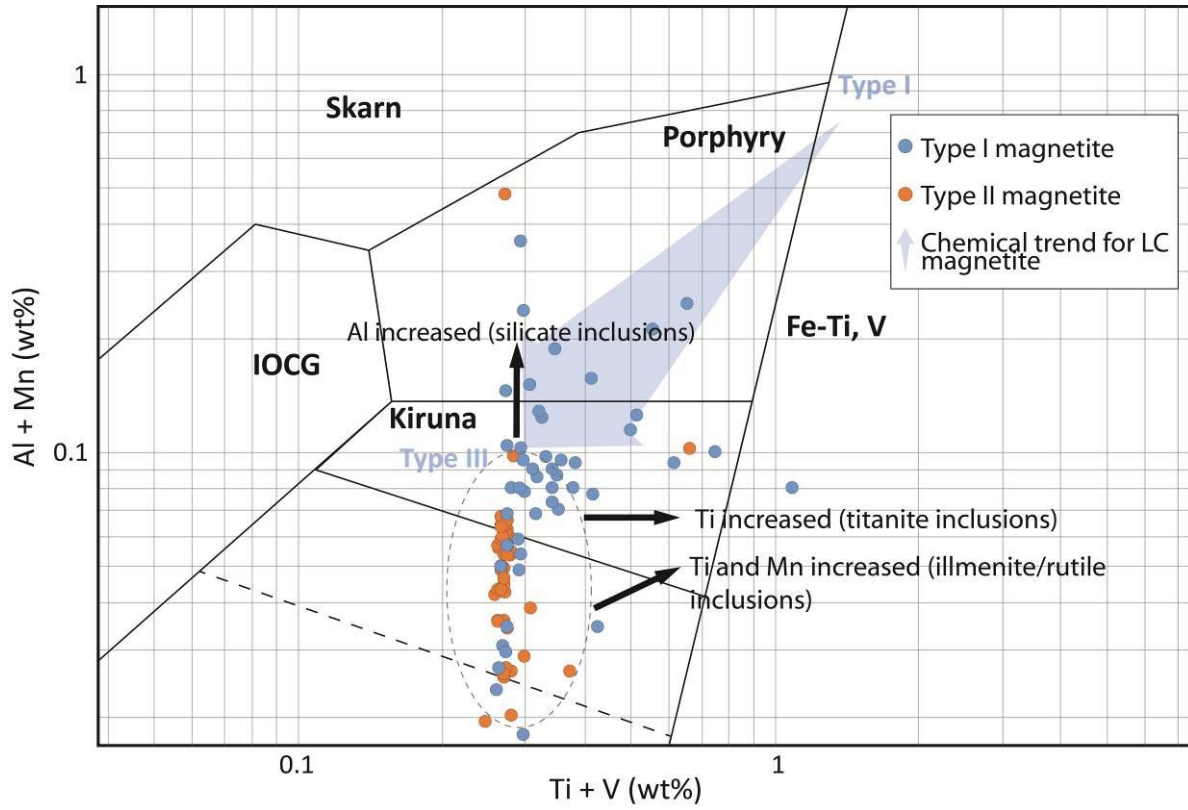


Figure 13

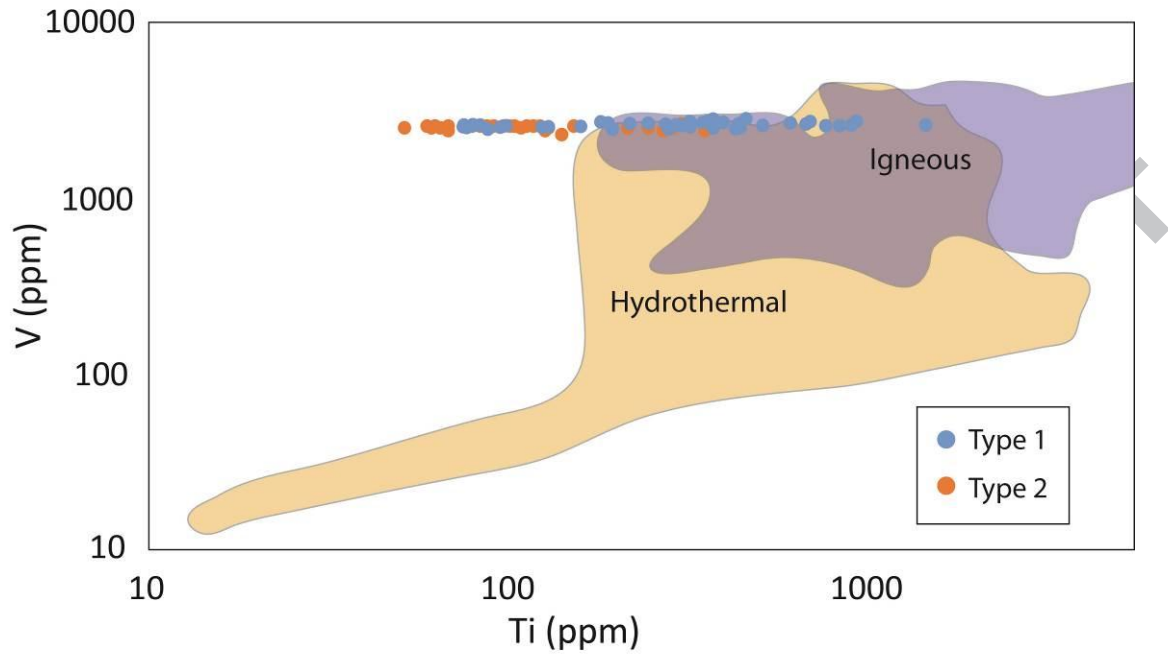


Figure 14

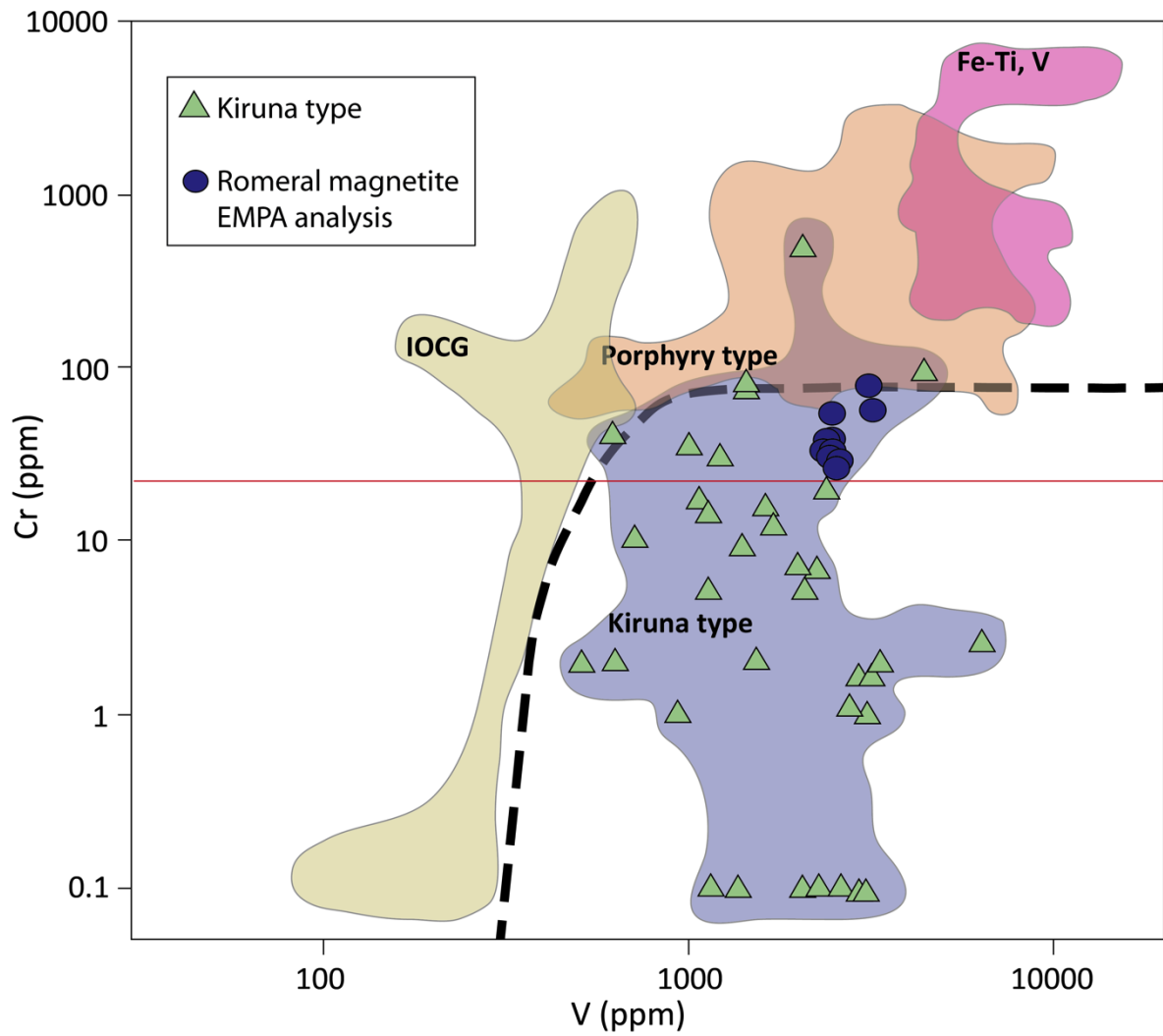


Figure 15

ACCEPTED

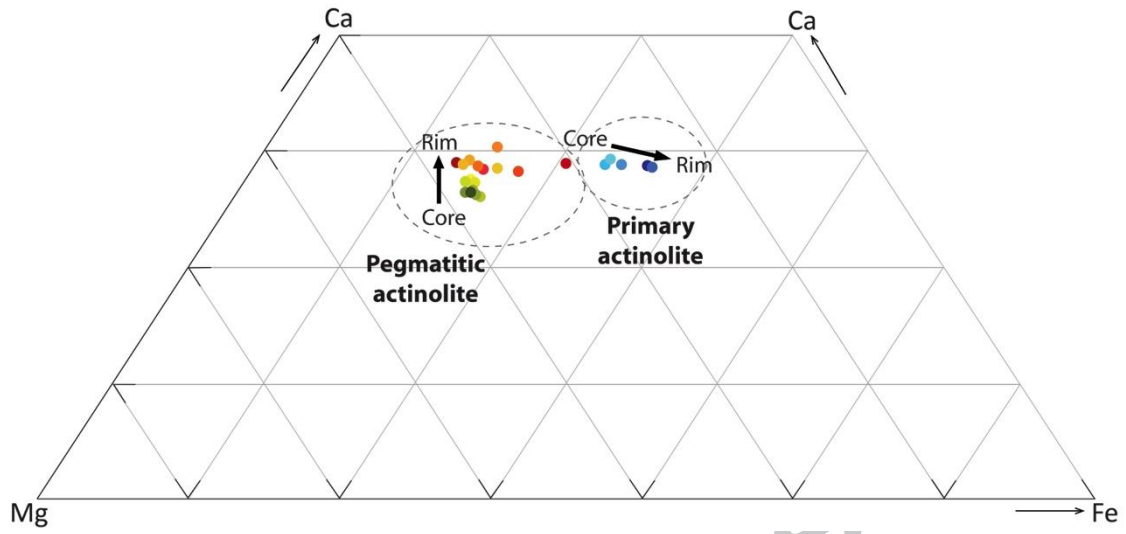


Figure 16

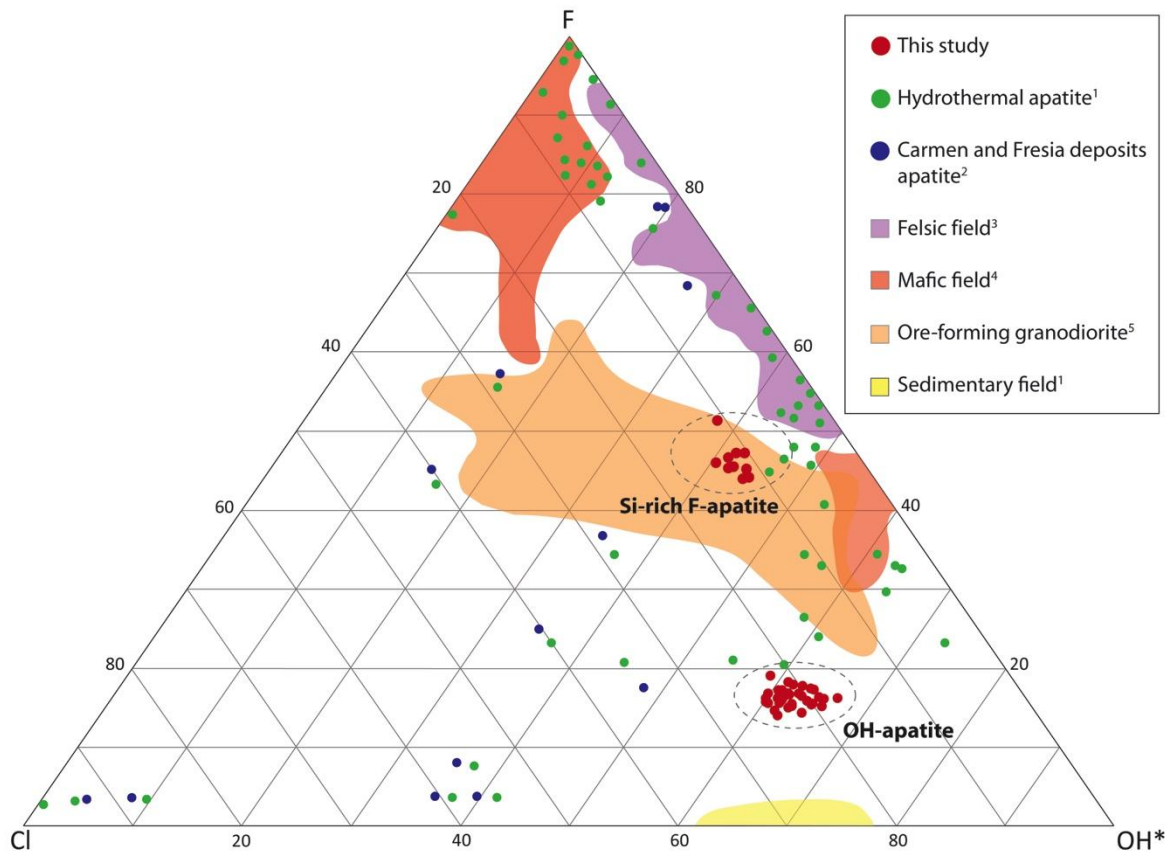


Figure 17

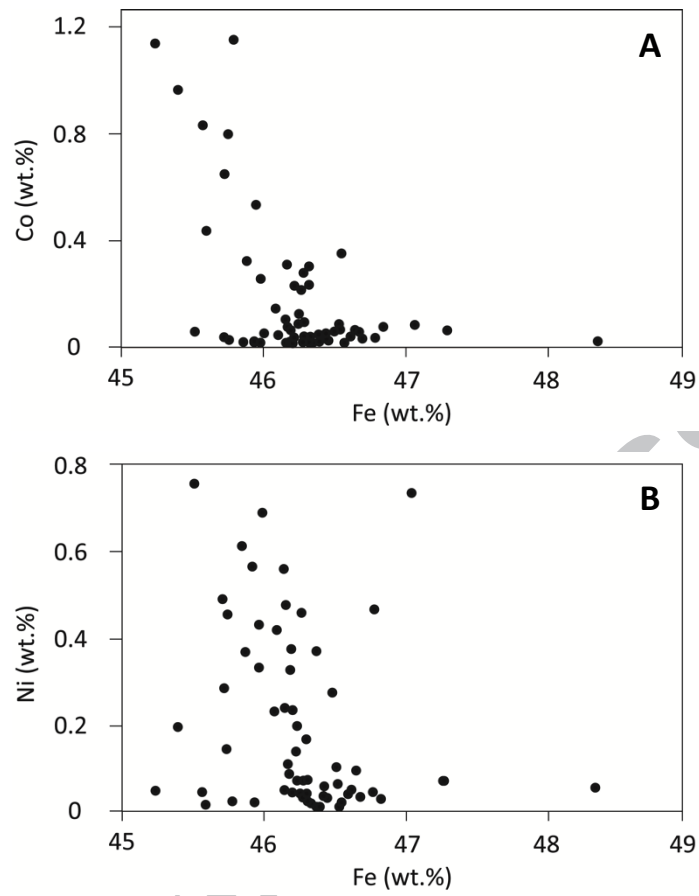


Figure 18

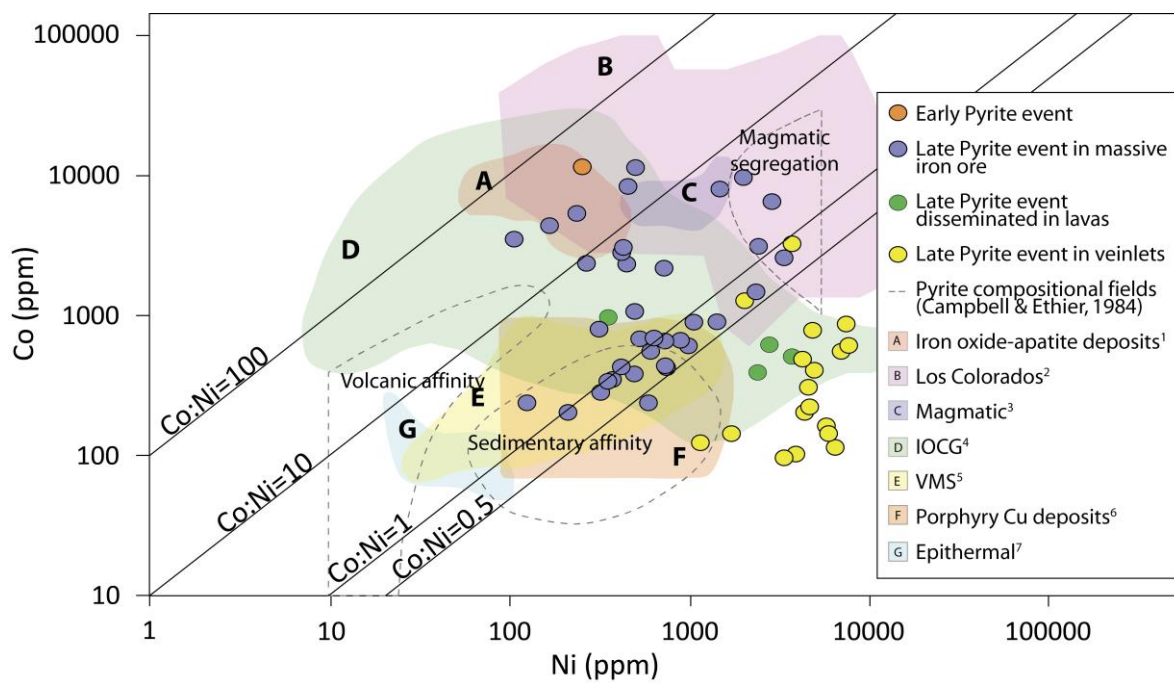


Figure 19

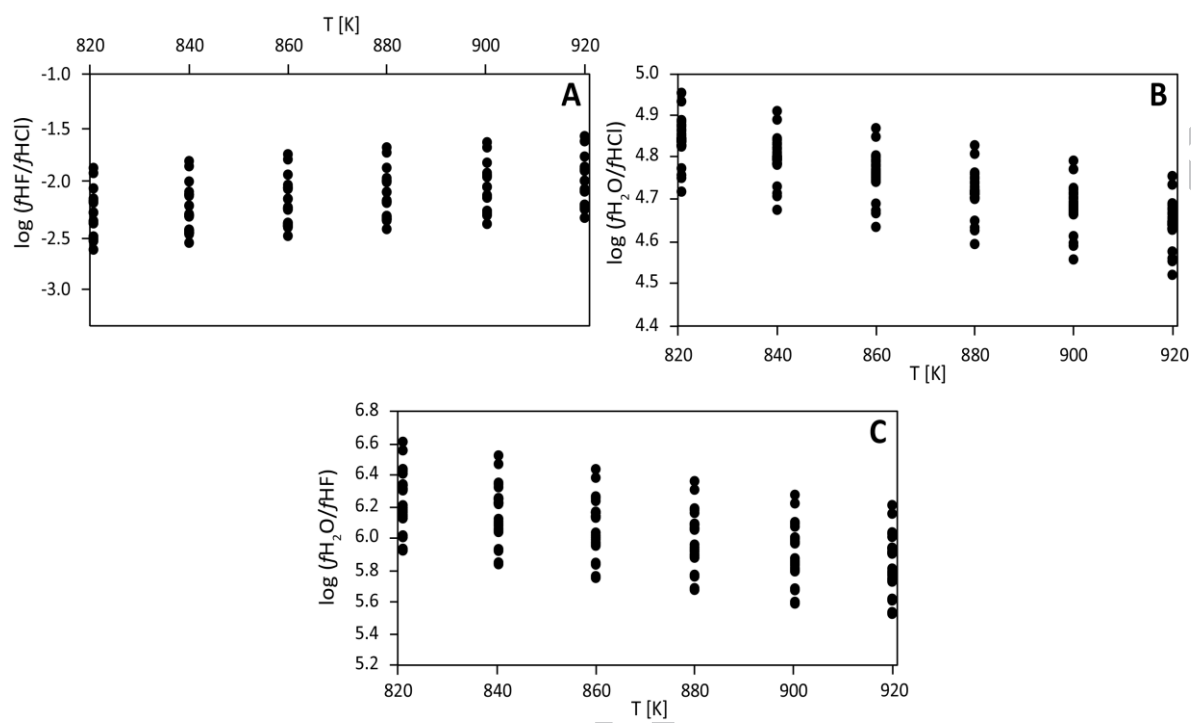


Figure 20

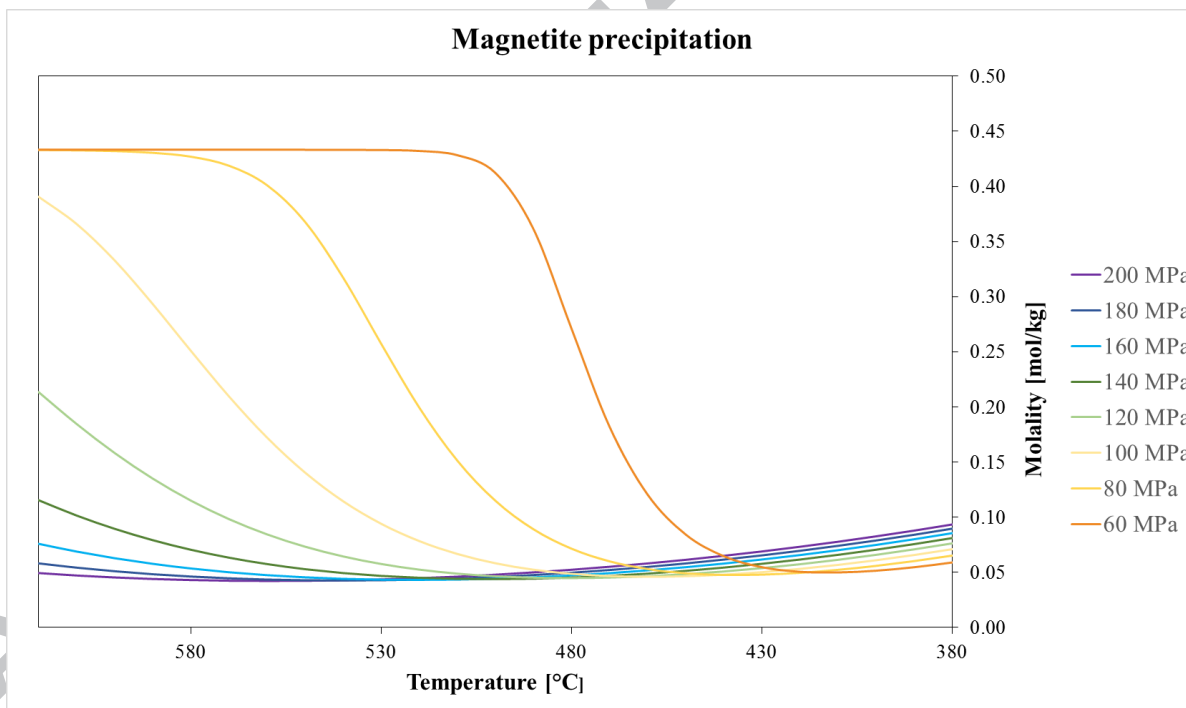
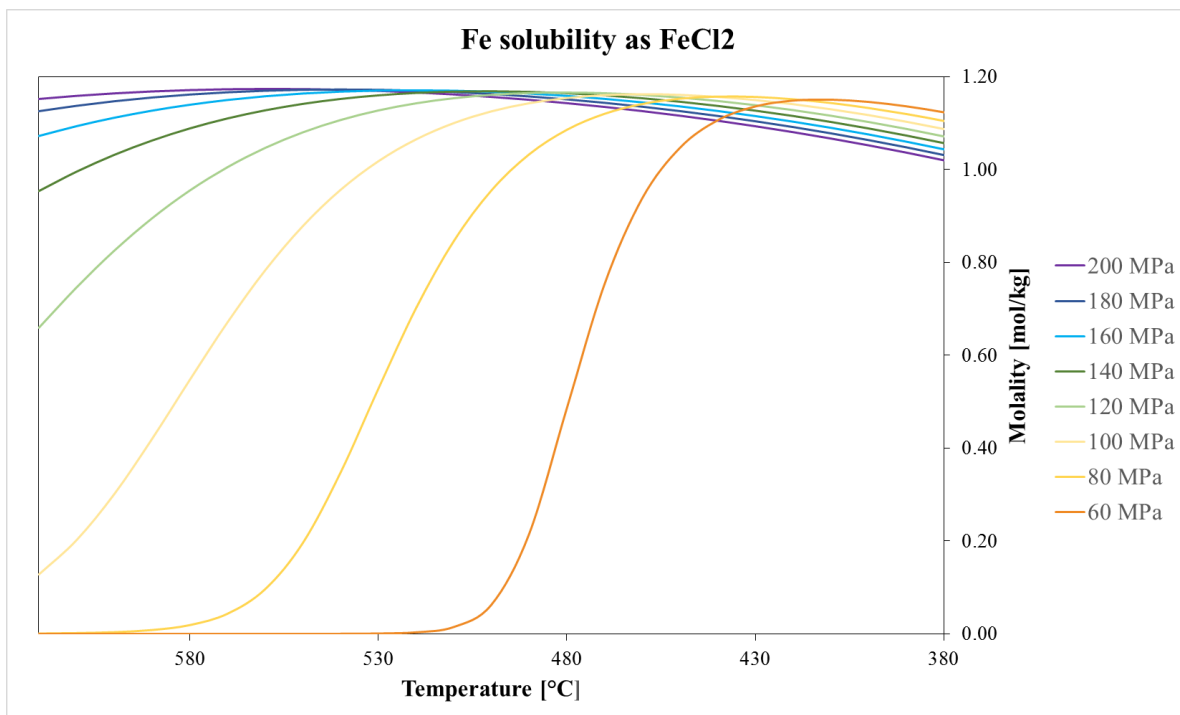


Figure 21

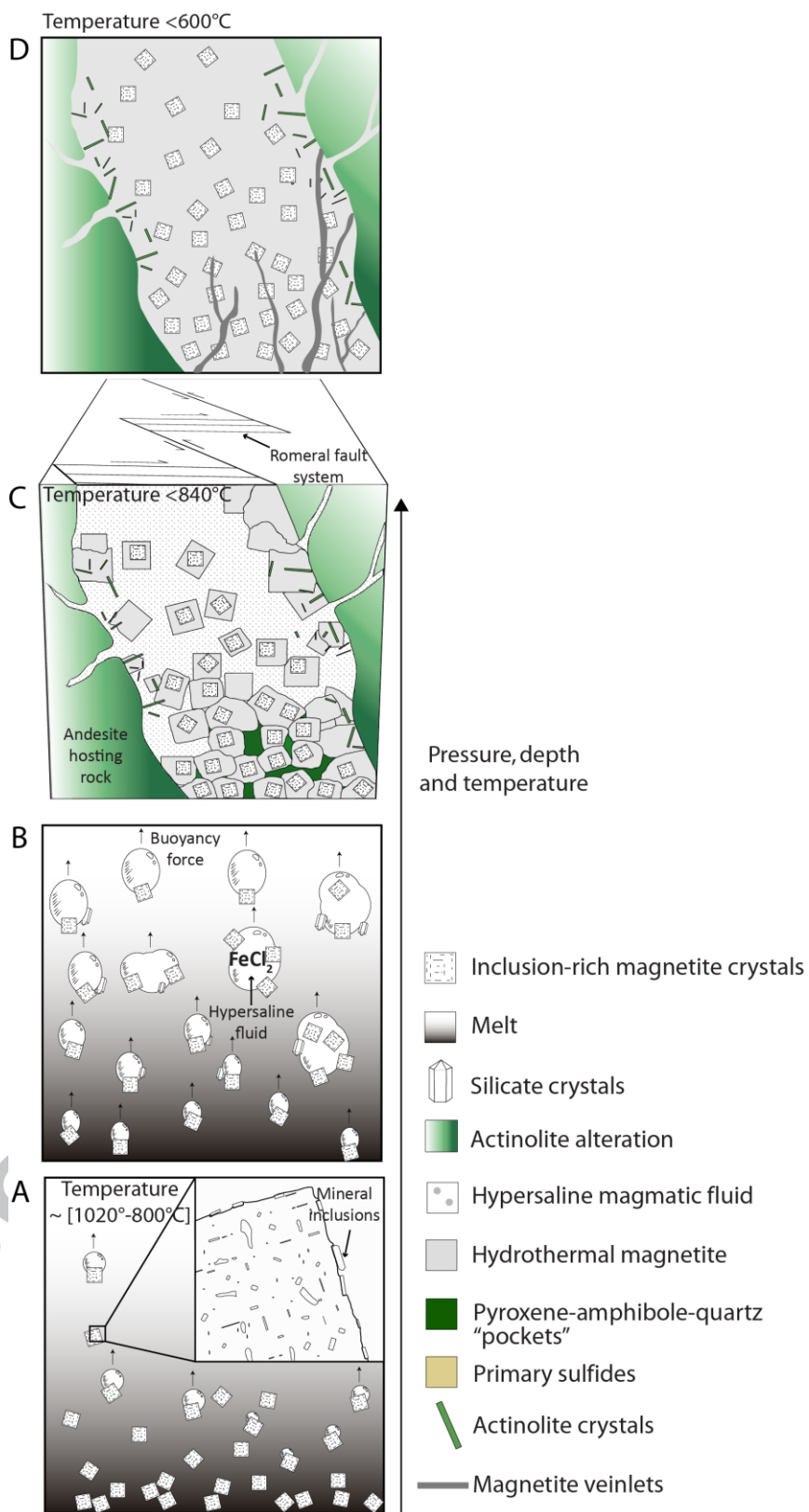


Figure 22